

Paleoseismology of the 2016 M_W 6.1 Petermann earthquake source: Implications for intraplate earthquake behaviour and the geomorphic longevity of bedrock fault scarps in a low strain-rate cratonic region

Tamarah Rosellen King^{1,2}  | Mark Quigley¹  | Dan Clark³ 
 Albert Zondervan⁴ | Jan-Hendrik May⁵  | Abaz Alimanovic¹

¹School of Earth Sciences, The University of Melbourne, Melbourne, Victoria, Australia

²COMET, Department of Earth Sciences, University of Oxford, Oxford, UK

³Geoscience Australia, Canberra, Australian Capital Territory, Australia

⁴Rafter Radiocarbon Laboratory, GNS Science, Lower Hutt, New Zealand

⁵School of Geography, The University of Melbourne, Melbourne, Victoria, Australia

Correspondence

Tamarah Rosellen King, School of Earth Sciences, The University of Melbourne, Melbourne, VIC 3010, Australia.
 Email: tamarah.king@earth.ox.ac.uk

Funding information

British Geological Survey; University of Melbourne; Australian Research Council, Grant/Award Number: DP170103350

Abstract

The 20 May 2016 M_W 6.1 Petermann earthquake in central Australia generated a 21 km surface rupture with 0.1 to 1 m vertical displacements across a low-relief landscape. No paleo-scarps or potentially analogous topographic features are evident in pre-earthquake Worldview-1 and Worldview-2 satellite data. Two excavations across the surface rupture expose near-surface fault geometry and mixed aeolian-sheetwash sediment faulted only in the 2016 earthquake. A 10.6 ± 0.4 ka optically stimulated luminescence (OSL) age of sheetwash sediment provides a minimum estimate for the period of quiescence prior to 2016 rupture. Seven cosmogenic beryllium-10 (^{10}Be) bedrock erosion rates are derived for samples < 5 km distance from the surface rupture on the hanging-wall and foot-wall, and three from samples 19 to 50 km from the surface rupture. No distinction is found between fault proximal rates (1.3 ± 0.1 to 2.6 ± 0.2 m Myr $^{-1}$) and distal samples (1.4 ± 0.1 to 2.3 ± 0.2 m Myr $^{-1}$). The thickness of rock fragments (2–5 cm) coseismically displaced in the Petermann earthquake perturbs the steady-state bedrock erosion rate by only 1 to 3%, less than the erosion rate uncertainty estimated for each sample (7–12%). Using ^{10}Be erosion rates and scarp height measurements we estimate approximately 0.5 to 1 Myr of differential erosion is required to return to pre-earthquake topography. By inference any pre-2016 fault-related topography likely required a similar time for removal. We conclude that the Petermann earthquake was the first on this fault in the last ca. 0.5–1 Myr. Extrapolating single nuclide erosion rates across this timescale introduces large uncertainties, and we cannot resolve whether 2016 represents the first ever surface rupture on this fault, or a > 1 Myr interseismic period. Either option reinforces the importance of including distributed earthquake sources in fault displacement and seismic hazard analyses.

KEY WORDS

cosmogenic ^{10}Be erosion rate, earthquake, earthquake recurrence, intraplate earthquake, OSL dating, paleoseismology, surface rupture, trenching

This is an open access article under the terms of the Creative Commons Attribution License, which permits use, distribution and reproduction in any medium, provided the original work is properly cited.

© 2021 The Authors. *Earth Surface Processes and Landforms* published by John Wiley & Sons Ltd.

1 | INTRODUCTION

Estimates of the slip rate and recurrence intervals for surface-rupturing faults are critical inputs to probabilistic fault displacement (e.g., Coppersmith & Youngs, 2000; Moss & Ross, 2011) and seismic hazard analyses (e.g., Allen et al., 2020; Stirling et al., 2012). Commonly, surface rupture traces and/or related surface deformation features (e.g., fault scarps, folds) produced in contemporary and/or pre-historic ('paleo') earthquakes are excavated by hand or machine to expose subsurface structural-stratigraphic relationships, from which earthquake displacements and chronologies may be characterized (e.g., Khajavi et al., 2016; Sieh, 1978; Stahl et al., 2016). Near-surface fault exposures in natural settings (e.g., stream cut-banks; Quigley et al., 2006; Sandiford, 2003) and progressive offsets of surface features (e.g., stream channels and terraces; Amos et al., 2011; Gold et al., 2017; Little et al., 2010) may also be utilized for this purpose. Determination of an earthquake recurrence interval requires estimates of the timing of multiple discrete seismic displacements, although other approaches that combine geodetic and seismologic data, slip rates, and earthquake scaling parameters are also used (e.g., Atwater et al., 2003; Dixon et al., 2003; Leonard & Clark, 2011; Nicol et al., 2016; Zielke, 2018). The accuracy and precision with which recurrence intervals may be estimated depends on many factors, including (i) the suitability of fault-related sediments and surface features for age dating, (ii) the analytical uncertainties associated with the age data, (iii) the epistemic uncertainties associated with interpretation and attribution of structural-stratigraphic data to distinct earthquakes at distinct times, and (iv) the assumption that the geologic record is a complete archive of seismic activity on the studied fault(s). Many paleoseismic studies are limited by several of these factors.

Australia has experienced 11 surface-rupturing earthquakes since 1968 (King et al., 2019; and references cited therein) that collectively comprise the richest domestic intraplate record of historical reverse-fault surface ruptures globally. Five of these earthquakes have been investigated using machine-dug (Clark & Edwards, 2018; Crone et al., 1997) or hand-dug (Clark et al., 2014, 2020; Lewis et al., 1981; this study) excavations combined with the structural-stratigraphic approaches outlined earlier. For four of these five events, structural and stratigraphic evidence for paleo-earthquakes is not recorded in the exposed Quaternary/Tertiary sediments and/or Precambrian bedrock. In one case, the Lake Surprise East (Tennant Creek) rupture (Crone et al., 1992), the excavated trench exposed a pre-existing bedrock scarp of ambiguous origin, and a non-seismic interpretation is equally permissible (King et al., 2019). It is therefore unresolved whether these earthquakes occurred on 'active' faults (e.g., faults with evidence of preceding Holocene or Pleistocene surface ruptures; Clark et al., 2008, 2012; Crone et al., 2003; Machette, 2000; Quigley, Clark & Sandiford, 2010), whether these faults were newly activated (e.g., along pre-existing planar structures) or newly created in these earthquakes (e.g., had no brittle failure prior to historical rupture; Clark & Edwards, 2018; Machette et al., 1993), or whether these faults exhibit incipient, emergent rupture behaviours (e.g., fault emergence at the ground surface through upward fault tip migration and fault propagation folding; Finch et al., 2003; Hardy & Finch, 2007; Livio et al., 2014, 2019; Tindall & Davis, 1999). Such distinctions bear directly on questions of how best to characterize seismic hazard in slowly deforming continental interiors (Allen et al., 2020; Clark, 2018;

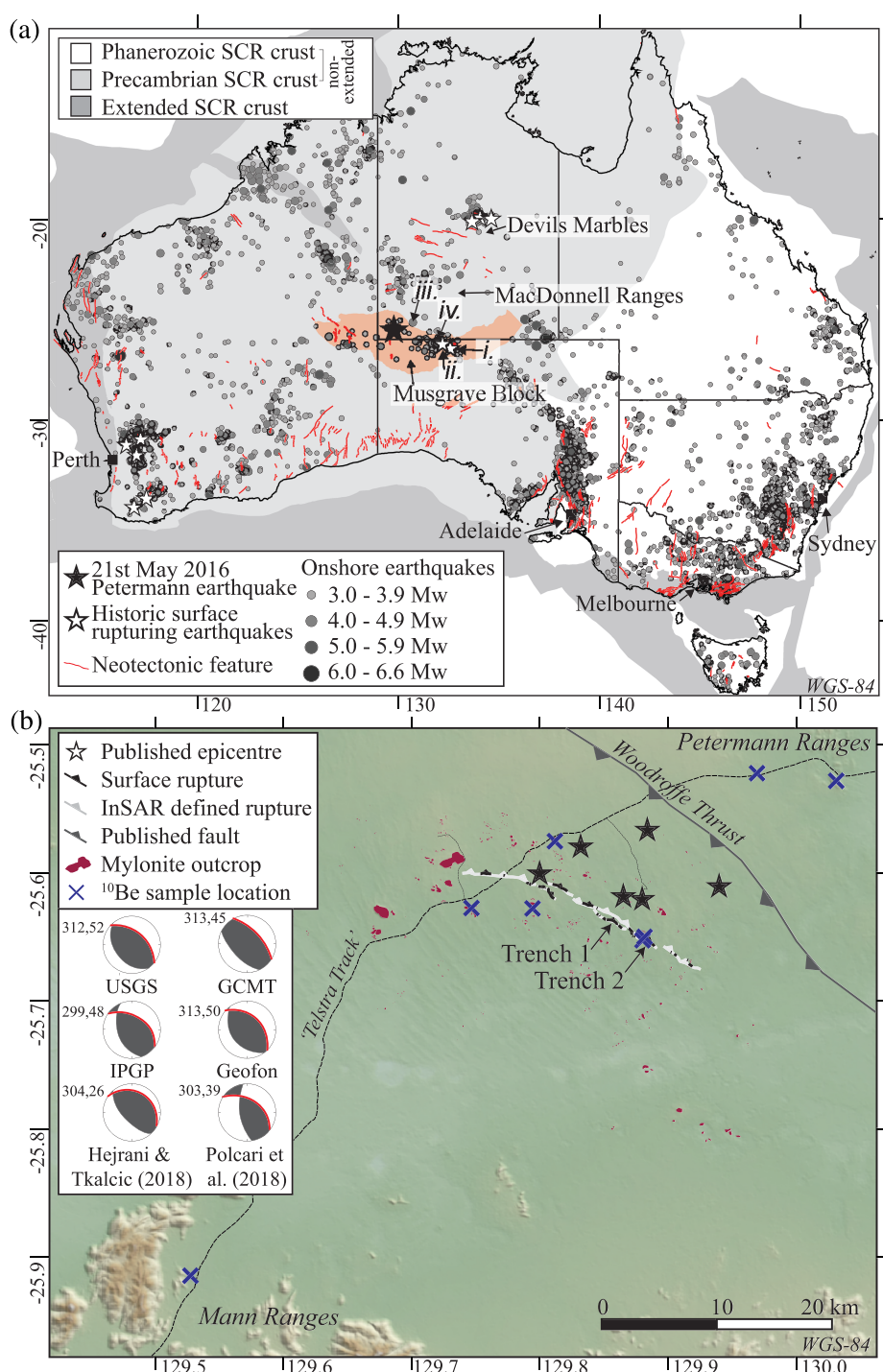
Clark et al., 2012; Leonard et al., 2007) and evaluate potential driving forces responsible for intraplate seismicity (Calais et al., 2005, 2016; Craig et al., 2016; Liu & Stein, 2016).

In slowly deforming continental interiors, fault recurrence data are often challenging to obtain because likely recurrence intervals for surface rupturing earthquakes (greater than several 10^4 to greater than 10^5 years) may exceed the age of available near-surface sediments (Clark et al., 2008, 2011, 2012; Crone et al., 1997), and/or may exceed the temporal range over which earthquake-associated sediments may be dated by radiocarbon (ca. 0–40 kyr; Ramsey, 2008) and optically stimulated luminescence (OSL) techniques (commonly less than 70 ka for U-Th-K (uranium, thorium, potassium) rich sediments in the Australian context; Clark, Griffin, et al., 2017; Quigley et al., 2006). Furthermore, landscape modification rates associated with erosion and/or sedimentation processes may exceed fault-slip rates associated with the maintenance of fault-associated topography (Hornblow et al., 2014). We attempt to tackle these challenges here by combining environmental effects observed in the 2016 M_w 6.1 Petermann earthquake (King et al., 2019) with a multi-methods approach aimed to quantify landscape evolution rates in the near-fault region. We integrate landscape analyses using satellite imagery (e.g., Worldview data) and beryllium-10 (^{10}Be) cosmogenic nuclide-derived erosion rate estimates with more typical structural-stratigraphic approaches (trenching) to expand the confidence of paleoseismic interpretations and the time-range over which such studies may be undertaken.

1.1 | Seismotectonic setting

Australia is one of the most seismically active Stable Continental Regions (SCRs) globally (Braun et al., 2009; Johnston et al., 1994; Sandiford & Quigley, 2009), with a rich historical record of surface-rupturing earthquakes (Clark et al., 2020; King et al., 2019). The identification of more than 360 faults and folds with topographic and/or geologic evidence for Quaternary earthquake displacement(s) extends contemporary seismicity over geological timescales (Figure 1; Allen, Leonard, et al., 2018; Clark, 2012; Clark et al., 2012; Quigley, Clark & Sandiford, 2010). Investigating earthquake surface rupture hazard is important in the Australian context for multiple reasons. Firstly, high-population urban centres (e.g., Adelaide, Melbourne and Sydney) and critical infrastructure (e.g., large dams, energy schemes, transport and utility corridors) are located near known and/or suspected Quaternary-active faults. The seismic risk is unknown for many of these faults; particularly the faults which are suspected of being active during the Quaternary. These uncharacterized faults present the largest potential seismic hazard in Australia. Secondly, the current national probabilistic seismic hazard assessment (NSHA18) (Allen et al., 2020) and seismic guidelines for large dams (ANCOLD (Australian National Committee on Large Dams), 2019) rely on sparsely resolved source-based inputs for faults. Finally, geologic data provides constraints on, and aids in, the development of new models to explain intraplate seismicity (Clark et al., 2016; Clark, Griffin, et al., 2017; Stirling et al., 2011). Within Australia these geological data require further investigation to prove useful, as they are complicated by preliminary evidence indicating highly episodic rupture recurrence behaviours, spatial and temporal earthquake clustering (Clark et al., 2012; Crone et al., 1997), and surface-rupturing earthquakes on faults

FIGURE 1 (a) Seismotectonic map of Australia showing cratonic regions (Leonard et al., 2014), historic onshore earthquakes from the NSHA18 catalogue (Allen, Leonard, et al., 2018), neotectonic features (Clark, 2012), historic surface rupturing earthquakes (King et al., 2019), geographic locations as discussed in text, and significant earthquakes in the vicinity of the 2016 Petermann earthquake (i), 1986 M_w 5.7 Marryat Creek (Machette et al., 1993) (ii), 2012 M_w 5.18 Pukatja surface-rupturing earthquakes (Clark et al., 2014) (iii), 1989 M_L 4.99 Uluru (Michael-Leiba et al., 1994) (iv), 2013 M_w 5.38 Mulga Park (Clark & McPherson, 2013). (b) Shaded relief map of region around the 21 May M_w 6.1 Petermann earthquake with published epicentres and surface rupture as in King et al. (2019), Woodroffe Thrust location (Scrimgeour et al., 1999), location of samples (also shown in Figure 2), trench locations and bedrock outcrops in the vicinity of the 2016 surface rupture as mapped from available satellite imagery [Color figure can be viewed at wileyonlinelibrary.com]



without clear evidence for analogous predecessors (Clark & Edwards, 2018; Clark et al., 2020; King et al., 2019).

1.2 | The 2016 Petermann earthquake

The M_w 6.1 Petermann earthquake occurred on 20 May 2016 at 03:44 Australian central standard time. It was located in the Proterozoic Musgrave Block of central Australia (Edgoose et al., 2004) with epicentre location estimates of -25.566°S , 129.884°E (USGS Earthquakes Hazards Program, <https://earthquake.usgs.gov/earthquakes/eventpage/us10005iyk#scientific>) and -25.58°S , 129.83°E (Geoscience Australia, <https://earthquakes.ga.gov.au/event/ga2016jyjxze>) (location uncertainty of 2.2 to 9 km radius; Figure 1). Additional epicentre locations are published by Global CMT (Ekström et al., 2012), GEOFON (<https://geofon.gfz-potsdam.de/>),

Polcari et al. (2018), and Hejrani and Tkalcic (2018) (centroid moment solution). There are no accurate hypocentre depth estimates (the closest seismometer is 166 km west) though a centroid moment tensor depth was estimated at 1 km (Hejrani & Tkalcic, 2018). All published focal mechanisms indicate an almost pure-reverse faulting event (Figure 1). Prior notable seismicity within 300 km of the Petermann epicentre includes two surface-rupturing earthquakes (1986 M_w 5.7 Marryat Creek, and 2012 M_w 5.18 Pukatja [Ernabella]; Clark et al., 2014; Machette et al., 1993), the 1989 M_L 4.99 Uluru earthquake (Michael-Leiba et al., 1994), and 2013 M_w 5.38 Mulga Park earthquake (Clark & McPherson, 2013; Figure 1; magnitudes from Allen, Leonard, et al., 2018)). No earthquakes greater than M_w 3.0 have been instrumentally recorded within a 50 km radius of the epicentre of the Petermann earthquake over the period of the instrumental record (see Leonard, 2008).

The Petermann earthquake generated a discontinuous surface rupture extending for a total length of 21 km, as identified from analysis of interferometric synthetic aperture radar (InSAR) data and field observations (Gold et al., 2019; King et al., 2018; Polcari et al., 2018; Wang et al., 2019; Figure 1). The surface rupture trace has an average strike of $294^\circ \pm 29^\circ$ (Attanayake et al., 2020). The rupture plane dips between 25° and 35° to the northeast as indicated by focal

mechanisms, modelled by InSAR, and mapped from surface data (Attanayake et al., 2020; Polcari et al., 2018; Wang et al., 2019; this study). The total length of discrete ground surface ruptures identified through field studies is 20 km (Gold et al., 2019; King et al., 2019). Measurements of vertical displacement across the discrete ground surface rupture and broader distributed deformation zone range from less than 0.1 m to greater than 1 m (Attanayake et al., 2020; Gold et al., 2019)

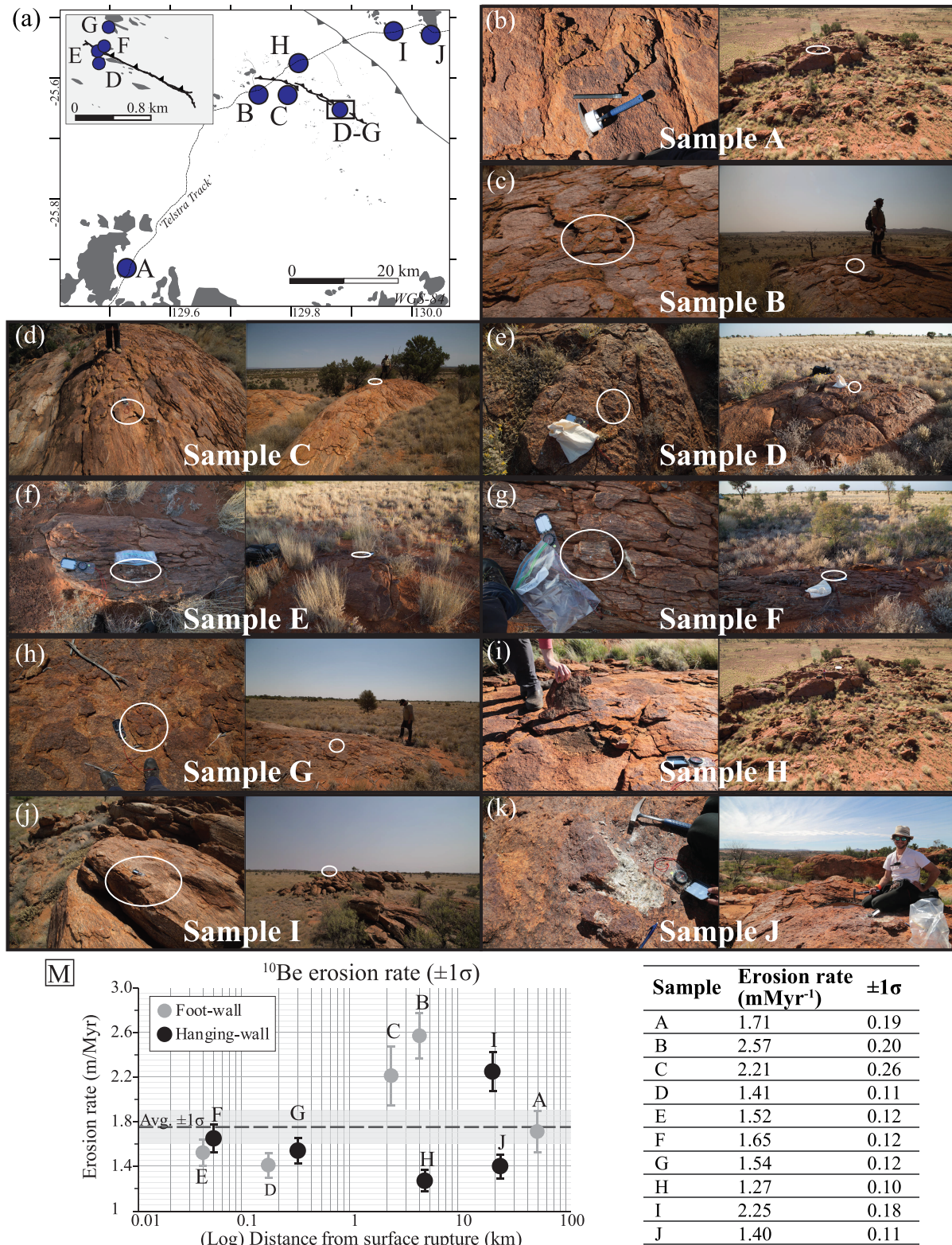


FIGURE 2 (a) Map of sample locations. (b-l) Photographs of each sample (Samples A–J) and outcrop (sample location circled in white, scale provided by field geologists or equipment). (M) Time-dependent erosion rate results with 1σ external uncertainty bounds (Balco et al., 2008; Lifton et al., 2014) for hanging-wall and foot-wall samples at distance from surface rupture trace, and table of results [Color figure can be viewed at wileyonlinelibrary.com]

with an average uplift of the hanging-wall of 23 cm relative to the foot-wall as measured at the surface rupture by a real-time kinematic global positioning system (RTK GPS) (Attanayake et al., 2020).

Hanging-wall bedrock outcrops within 5 km of the Petermann surface rupture experienced strong ground motion induced rock falls, *in situ* fracturing, and displacement of thin (2–5 cm thick) rock fragments sourced primarily from exfoliation sheets (as visible in most outcrop images of Figure 2 and described in King et al., 2018). Rock fall damage on foot-wall outcrops was only observed at less than 2 km distance from the surface rupture, and the intensity of bedrock fracturing and rock fragment displacements on the foot-wall was greatly reduced relative to hanging-wall outcrops (King et al., 2018).

The surface rupture trace obliquely intersects a 055° orientated and southwest-sloping (approximately –0.1%) line of intermittent drainage overlying a paleochannel (marked by section Y-Y' on Figure 3). The surface rupture has caused discrete offset of this paleo-drainage, increasing gradients in the hanging-wall and reducing gradients in the foot-wall. Distributed deformation and uplift of the hanging-wall, as observed in satellite data of Gold et al. (2019) up to 5 km from the surface rupture, has also caused a reduction in gradient for the distal hanging-wall. This mild topographic perturbation could theoretically propagate into associated south to southwest flowing tributaries along the fault and enhance erosion of the hanging-wall by increasing stream power and concentrating erosion proximal to the

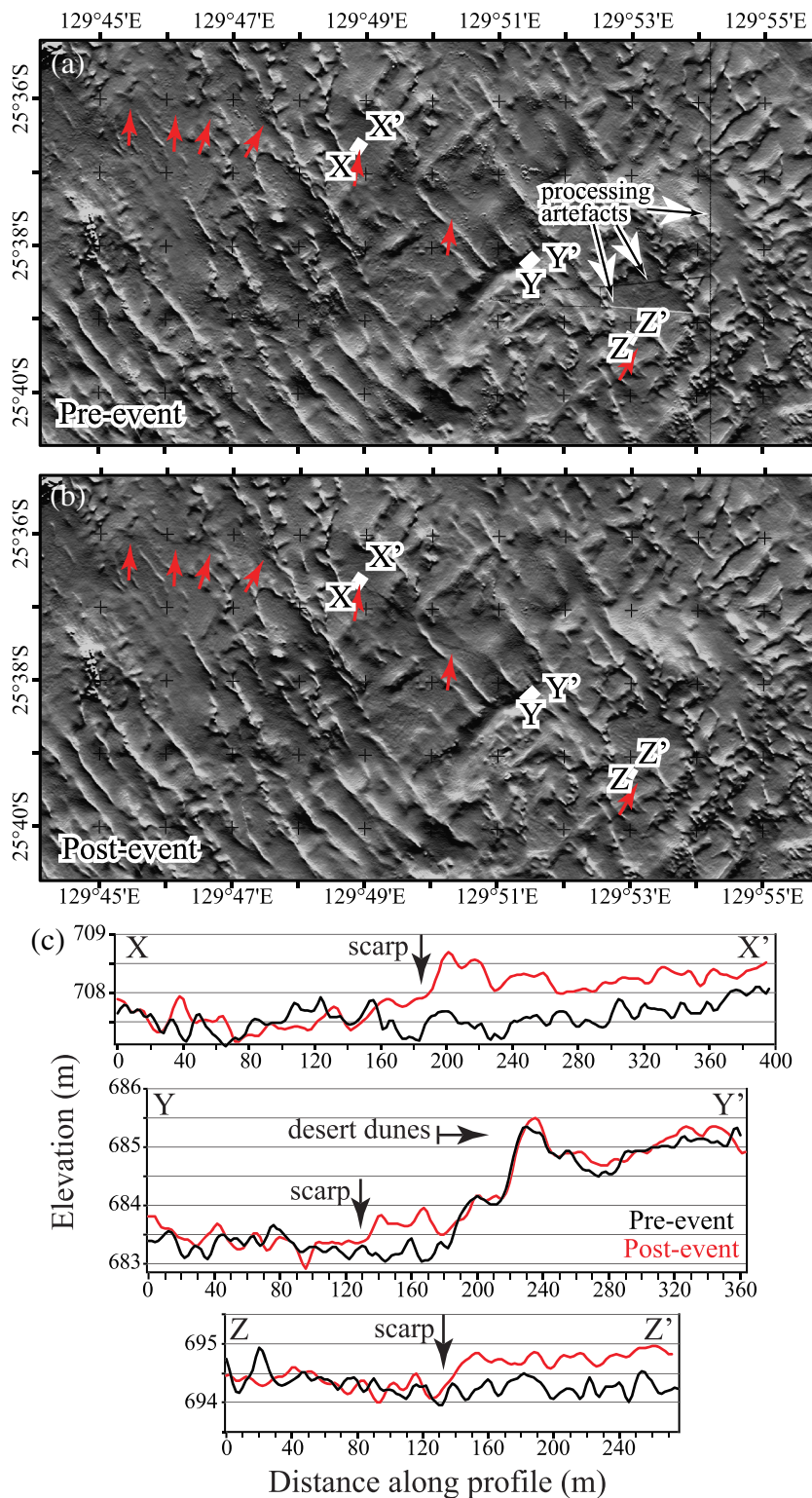


FIGURE 3 Pre- and post-Petermann earthquake 2 m resolution digital elevation models (DEM data from Gold et al. (2019)). Hill shading simulates illumination from the north. (a) Pre-earthquake DEM (derived from March and June 2014 Worldview-1 images), (b) post-event DEM (derived from October and November 2016 Worldview-2 images), (c) topographic profiles derived from pre- (black) and post- (red) earthquake DEM data. Red arrows in (A) and (B) indicate prominent scarp segments visible in (B). Profiles X-X', Y-Y' and Z-Z' locations shown by white lines in (A) and (B) [Color figure can be viewed at wileyonlinelibrary.com]

fault scarp (Hanks, 2000). Erosion has been locally enhanced by bedrock shattering, rock fragment displacement (Figure 2), and rockfalls, particularly on the hanging-wall where coseismic shaking damage was more intense (King et al., 2018).

2 | METHODS

2.1 | Analysis of Worldview-1 imagery and elevation model

For our topographic analysis we use the pre- and post-Petermann earthquake digital elevation models (DEMs) produced by Gold et al.

(2019). These were derived using pre-event (March and June 2014) and post-event (October and November 2016) in-track stereo 0.5 m resolution panchromatic WorldView-1 and WorldView-2 images (©2019, DigitalGlobe) using the Surface Extraction from TIN-based Searchspace Minimization software (Noh & Howat, 2015) running on the University of Iowa Argon supercomputer. The DEMs are available at <https://doi.org/10.5066/P9353101>, and the processing techniques are described in the supplementary information provided by Gold et al. (2019), available at <https://doi.org/10.1029/2019GL084926>. The data were visualized in the ER Mapper software by applying a hillshade algorithm simulating the sun shining from the north (Figure 3). This sunshade azimuth has the effect of highlighting the topography relating to the scarp and local dune trends, while at the

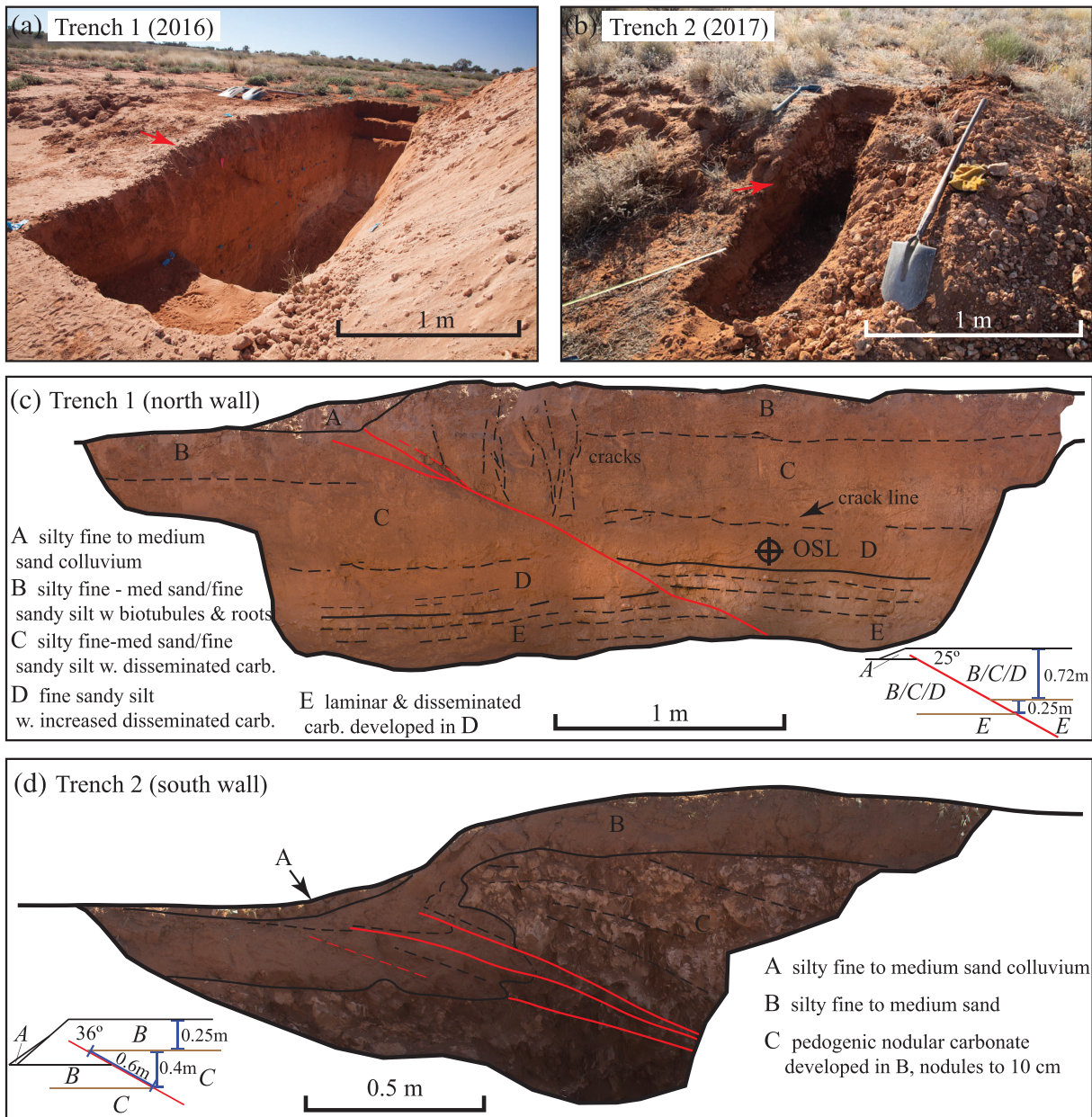


FIGURE 4 Field photographs and logs of trenches across the Petermann earthquake surface rupture. (a) Photograph of Trench 1 ($-25.637, 129.856$; WGS84) showing disseminated carbonate horizon displaced across the fault plane, looking north (red arrow indicates the fault tip), (b) photograph of Trench 2 ($-25.654, 129.884$; WGS84) showing nodular carbonate horizon displaced across the fault plane, looking south (red arrow indicates the fault tip), (c) log of Trench 1 including location of OSL sample and schematic showing measured offsets and dip, (d) log of Trench 2 including schematic showing measured offsets and dip. Note that images in (b) and (d) have been reflected to match (a) and (c). Trench photomosaics in (c) and (d) were produced using structure from motion techniques from multiple field photographs in the Agisoft Photoscan software and some artefacts are visible. Additional images of each trench without photogrammetry artefacts are published in Figures S1 and S2 [Color figure can be viewed at wileyonlinelibrary.com]

same time minimizing the visual effect of along-track striping artefacts common to the WorldView-2 sensor. Topographic profiles were constructed through the pre- and post-event data at three locations across the Petermann earthquake surface rupture for comparison (Figure 3).

2.2 | Fieldwork and trenching

Fieldwork was conducted along and across the May 2016 Petermann surface rupture in June 2016 and September 2017 (see King et al., 2018, for more details). We hand-excavated two trenches across the surface rupture trace. In 2016 we excavated Trench 1 within the aforementioned paleo-channel (Figures 1 and 3) to constrain the near-surface fault dip and characterize structural–stratigraphic relationships. This trench was reopened in September 2017 to obtain an OSL sample from faulted sediments.

Trench 2 (Figure 1) was excavated in September 2017 3.5 km southeast of Trench 1 in an interdune sand-plain with shallow and outcropping crystalline bedrock and calcrete. The base of Trench 1 was hard calcrete (see Section 3.2) and our aim for Trench 2 was to potentially expose bedrock or the base of the calcrete layer. This may have helped to identify any faulting preserved in bedrock, or stratigraphy below and pre-dating the calcrete layer. Trench 2 also provided confidence to our understanding of near-surface fault geometry.

2.3 | Optically stimulated luminescence

OSL samples were collected by driving a stainless-steel tube into unconsolidated sediments at 0.7 m depth (Figure 4, Table 1) with additional sediment surrounding the tube collected to determine the concentration of dose-relevant elements (i.e., U, Th, K) by inductively coupled plasma mass spectrometry (ICP-MS). The material extracted from the inner part of the tubes was prepared for measurement of the equivalent dose (D_e) at the University of Melbourne. Sample preparation was conducted under red-light conditions and followed standard procedures (e.g., Wintle, 1997) including separation of the 180–212 µm fraction by wet sieving, elimination of carbonates and organics using hydrochloric acid (HCl) and hydrogen peroxide (H_2O_2) isolation of the quartz fraction using heavy liquid separation, and etching with 40% hydrogen fluoride (HF) for 45 min followed by HCl treatment. We apply an infrared-depletion test to check for the presence of feldspar (Duller, 2003) followed by a single-aliquot regeneration (SAR) protocol from Murray and Wintle (2000) to determine D_e values for 24 sample aliquots (1 mm) (Table 1). Measurements were conducted on a Risø TL/OSL DA-20 reader equipped with blue diodes and Hoya U-340 detection filters using regenerative and test dose preheats of 180°C for 10 s and 180°C for 5 s, respectively. After inspection of D_e values, paleo-dose calculation was based on the Central Age Model (CAM, Galbraith et al., 1999). Dose rate and a final OSL age (Table 1) were calculated using the ADELE software developed by D. Degering (ADELE dose rates are based on Appendix H in Aitken, 1985). Cosmic dose rate (Table 1) was calculated using present-day depth and correcting for geographical position following the approach in Adamiec and Aitken (1998). Present-day water

Latitude	Longitude	Depth (m)	Moisture (%) ± 1σ	Uranium (ppm) ± 1σ	Thorium (ppm) ± 1σ	Potassium (%) ± 1σ	Dose rate (Gy ka ⁻¹) ± 1σ	D_e (Gy) ± 1σ	Age (ka) ± 1σ			
OSL1	-25.638	129.857	0.7	8.2 ± 3.0	3.458 ± 0.034	4.468 ± 0.026	0.786 ± 0.004	1.93 ± 0.04	24/24	12.2 ± 1.9	20.43 ± 0.53	10.57 ± 0.37

TABLE 1 Optically stimulated luminescence (OSL) sample data and results

^aEquivalent dose based on Central Age Model (Galbraith et al., 1999).

TABLE 2 Beryllium-10 (^{10}Be) sample data and erosion rate results

R_X^a (km)	Field code	Laboratory Code (UoM)	Laboratory Code (GNS)	Sampling date	Latitude	Longitude	Elevation (m a.s.l.)	Thickness (cm)	Shielding factor ^b	^{9}Be Carrier (μg)	$^{10}\text{Be}/^{9}\text{Be}^c$ (10^{-12}) $\pm 1\sigma$ error	^{10}Be Concentration (10^8 atom g^{-1}) $\pm 1\sigma$ error	Erosion rate ^d (m Myr^{-1}) $\pm 1\sigma$ error ^e		
Foot-wall	49.5	A	Be 0	Be3962	14 June 2016	-25.91	129.53	724	3	0.99988	18.65	373.2	1.23 \pm 0.09	1.64 \pm 0.12	1.71 \pm 0.19
4.0	B	Be 8	Be3970	22 September 2017	-25.63	129.75	739	3	1.00000	20.58	410.6	0.88 \pm 0.03	1.16 \pm 0.04	2.57 \pm 0.20	
2.2	C	Be 7	Be3969	17 September 2017	-25.63	129.79	734	5	0.96869	19.99	364.5	1.04 \pm 0.09	1.26 \pm 0.11	2.21 \pm 0.26	
0.16	D	Be 4	Be3966	21 September 2017	-25.65	129.88	692	5	1.00000	20.33	405.3	1.39 \pm 0.03	1.84 \pm 0.05	1.41 \pm 0.11	
0.04	E	Be 5	Be3967	21 September 2017	-25.65	129.88	692	2	0.92359	16.77	399.2	1.04 \pm 0.03	1.65 \pm 0.04	1.52 \pm 0.12	
Hanging-wall	0.05	F	Be 6	Be3968	21 September 2017	-25.65	129.88	692	7	0.99530	18.09	412.2	1.04 \pm 0.02	1.58 \pm 0.04	1.65 \pm 0.12
0.3	G	Be 3	Be3965	20 September 2017	-25.65	129.88	696	6	0.99931	20.31	389.6	1.34 \pm 0.03	1.70 \pm 0.04	1.54 \pm 0.12	
4.5	H	Be 1	Be3963	12 June 2016	-25.58	129.81	735	3	1.00000	21.10	397.9	1.69 \pm 0.03	2.12 \pm 0.05	1.27 \pm 0.10	
19.0	I	Be 9	Be3971	23 September 2017	-25.52	129.97	716	6	0.99968	20.08	411.8	0.92 \pm 0.03	1.25 \pm 0.04	2.25 \pm 0.18	
22.5	J	Be 2	Be3964	13 June 2016	-25.53	130.03	736	3	0.99982	20.61	357.2	1.69 \pm 0.03	1.95 \pm 0.04	1.40 \pm 0.11	
Processing blank	K	Be 10	Be3972	Blank						0	412.1	0.008 \pm 0.002			

^aHorizontal distance from surface rupture to site.^bDensity assumed to be 2.7 g cm^{-3} (i.e., typical granite).^cIsotope ratios measured with XCAMS (Zondervan et al., 2015) using primary standard 0–5–4. $^{10}\text{Be}/^{9}\text{Be} = 2.851 \cdot 10^{-12}$ atom atom $^{-1}$ (Nishizumi et al., 2007).^dFrom G. Balco's ^{10}Be erosion rate calculator V3 (https://hes.ess.washington.edu/math/v3/v3_erosion_in.html), 'LSDn' time-dependent production rate (N. Lifton et al., 2014).^eQuoted errors represent both analytical uncertainty and model uncertainty associated with the chosen production rate model (Balco et al., 2008).

content and the field hydrological context were used to estimate average water content (Table 1) during sediment burial.

2.4 | Beryllium-10 cosmogenic nuclide erosion rates

Seven bedrock samples were collected for ^{10}Be cosmogenic nuclide erosion rate analysis along an 8.5 km long traverse approximately perpendicular to the 2016 surface rupture (Figure 2). Three additional samples were collected distal to the surface rupture (19–50 km) to provide proxies for background erosion rate (Figure 2). Samples were obtained by hammer and chisel from sub-horizontal weathered surfaces at the top of bedrock outcrops (Figure 2). Given the low relief, topographic shielding was minimal (Supporting Information Table S3). Sample thicknesses were recorded in the field (Table 2).

Samples A and J were collected to provide estimates of regional background erosion rates from the top of granite outcrops within the Mann Ranges (43 km southwest of the surface rupture and 20 m above sand plain) and Petermann Ranges (20 km northeast of the surface rupture and 50 m above sand plain) (Figure 2). Sample I was collected from a low (5 m above adjacent sand plain) granitic outcrop on the hanging-wall of the 2016 rupture and the foot-wall of the Woodroffe Thrust (Figures 1 and 2). The outcrop had fewer exfoliation sheets than all other sampled outcrops and thus appeared ‘fresher’ (i.e., a younger surface). This sample was analysed to potentially provide a maximum erosion rate for the area, given the fresh appearance of the outcrop. Samples B, C, and H were collected from large granitic outcrops less than 5 km from the surface rupture on both the hanging-wall and foot-wall (Figure 2). Samples D, E, F, and G were collected from low-lying (less than 1 m high) granitic mylonite outcrops within 500 m of the 2016 Petermann rupture on the hanging-wall and foot-wall (Figure 2). These samples came from similar outcrops with similar geomorphic settings (an inter-dune sand-plain region). Samples D, E, F, B and H, were collected to provide near-rupture constraints on erosion rates that might record evidence of paleoseismic activity.

Quartz was extracted from bedrock samples at the University of Melbourne using standard rock crushing, magnetic and heavy mineral separation techniques. Separation of Be from quartz grains was conducted at the University of Melbourne, following the method described in Quigley et al. (2007). The $^{10}\text{Be}/^{9}\text{Be}$ isotopic abundance ratio of the beryllium oxide samples was measured with XCAMS, the Accelerator Mass Spectrometry facility at GNS Science in New Zealand (Zondervan et al., 2015) (details in Table S4). Beryllium-10 erosion rates (Table 2) were calculated using version 3 of G. Balco’s online erosion rate calculator (last accessed in December 2019; https://hess.ess.washington.edu/math/v3/v3_erosion_in.html) (input data in Table S2). Reported data (Table 2) follow the recommended protocol of Frankel et al. (2010) and Dunai and Stuart (2009). Erosion rates reported in Table 2 are derived based on time-varying production rates modelled by Lifton et al. (2014) (further details on the erosion rate calculator website). Other stationary and time-variant model estimates (Lifton et al., 2008; Stone, 2000) are reported in Table S1. The latter deviate no more than 5% from the reported rates and are not discussed further.

Our erosion rate data combined with offset measurements of the Petermann surface rupture (Attanayake et al., 2020; Gold et al., 2019) provide an opportunity to quantify the potential time required to erode a scarp and uplifted topography in this bedrock-dominated landscape. To do this we make a number of assumptions. Firstly, we propose that the long-term post-earthquake hanging-wall (scarp) erosion rate may be approximated by the maximum ^{10}Be erosion rate observed in our sample cohort (Table 2). We acknowledge that past and future scarp degradation could involve a diversity of erosional mechanisms (e.g., alluvial and aeolian mechanical weathering, *in situ* chemical weathering) in rock and sediment that vary in time and space and thus acknowledge large epistemic uncertainties are inherent in this assumption. Secondly, we assume that our average and minimum ^{10}Be erosion rates (Table 2) represent long-term erosion rate estimates for the foot-wall. And finally, we assume that the differential erosion rates (ΔE ; Figure 5b) obtained from subtracting the average and minimum rates from the maximum rate provide crude proxies for the rate at which the hanging-wall re-achieves topographic

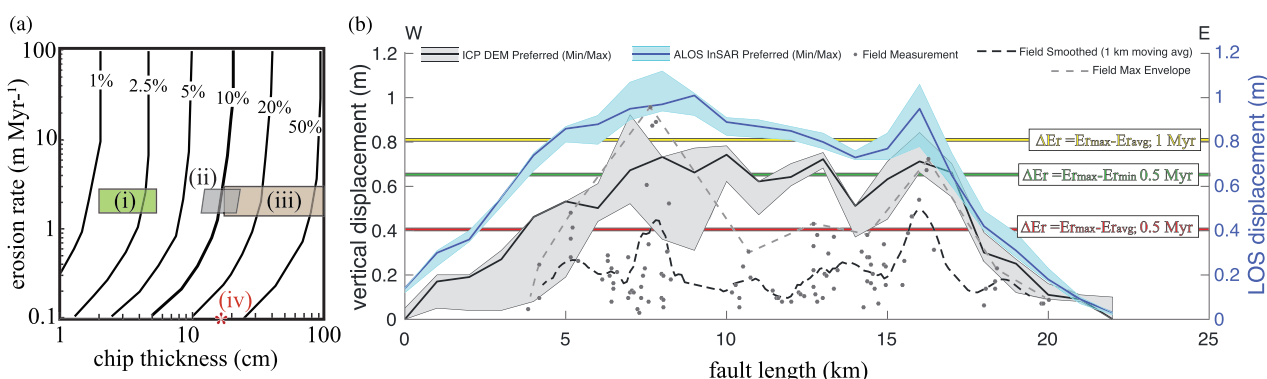


FIGURE 5 (a) Graph of erosion rate versus rock sheet/fragment thickness, where lines represent 1σ standard deviation in steady-state erosion rate for varying sheet thickness and mean erosion rate. Description of Boxes (i), (ii), (iii) and point (iv) as described in the text. Figure adapted from Figure 6a, Small et al., 1997 (b) Estimates for differential erosion rates (where $E_{r\max} - E_{r\min} = 1.3 \text{ mMyr}^{-1}$ and $E_{r\max} - E_{r\text{avg}} = 0.82 \text{ mMyr}^{-1}$) plotted against available vertical offset measurements (from field and remote-sensing data Figure 3; Gold et al. (2019)) to indicated the potential time required to erode the scarp and uplifted topography [Color figure can be viewed at wileyonlinelibrary.com]

equilibrium with the foot-wall (i.e., the fault scarp is denuded to a low slope feature indistinct from regional topography, and thus is no longer recognizable as a distinct, linear, stepped topographic anomaly that could be attributed to ground surface rupture). We use Equation (1): $1 \text{ m} - x \text{ Myr} * (\text{Er}_{\max} - \text{Er}_{\min \text{ or avg}})$ to estimate the residence of a 1 m high scarp in the landscape (note that offsets of $\approx 1 \text{ m}$ are only observed in the central 10 km of the scarp; Figure 5b).

Applying our erosion rate results in this way requires assumptions about how long the surface has been exposed, and that erosion rate has been constant through time (i.e., steady-state erosion). The steady-state erosion assumption is often supported through estimating a timescale for which a calculated erosion rate average is representative, in combination with geomorphological evidence. The sampled surface may be assumed to have been eroding at a constant rate over a timescale represented by Equation (2): Λ / ε , where ε is the rate of erosion and Λ is attenuation length. This represents the time required to erode a layer of thickness equal to the attenuation length and assumes no contradictions from field observations and geomorphological arguments (further explored in the Discussion section). The ratio Λ / ε is, to first order, approximated by the ratio between concentration N and production rate P of the cosmogenic isotope (Granger et al., 1996).

Here we aim to constrain the time-range over which those assumptions, and therefore our erosion rates, are applicable. This time-range is in practice limited by a combination of external processes (removal of overlying rock through erosion, attenuation of cosmic-ray particles by that material, radiometric decay). For the specific case of this study, the dominant external process is best described by gradual removal of overlying material. It is unlikely that these samples have experienced an abrupt change from deep burial to (near-)surface exposure on the timescale of the ^{10}Be half-life ($T_{1/2} \approx 1.4 \text{ Myr}$, Nishiizumi et al., 2007) although we do not evaluate the possibility of Plio-Quaternary regolith stripping in detail.

3 | RESULTS

3.1 | Analysis of pre-Petermann earthquake Worldview-1 imagery and elevation model

The Petermann Ranges earthquake ground surface rupture transects topographically subdued landscapes of the central Australian shield plain (Mabbutt, 1988; Figures 1 and 3) that include isolated granite and gneiss hills (inselbergs) of the Petermann and Mann Ranges (e.g., Edgoose et al., 2004; Figure 1) rising above the surrounding flat to gently undulating Cenozoic erosional surface. Moderately weathered mylonite occurs at or within $\sim 4 \text{ m}$ of the surface (King et al., 2018; Figure 1) suggesting the landscape was stripped of weathering products (i.e., saprolite) before the pre-Quaternary onset of aridity (e.g., Fujioka & Chappell, 2010). Sediments overlying bedrock are typically skeletal and related to sheetwash and aeolian processes, except where Tertiary paleo-valley systems contain several tens of metres of aeolian, fluvial, lacustrine and chemical sediments (e.g., Bell et al., 2012). The shield plain is extensively overlain by a field of southeast-trending mid- to late-Pleistocene longitudinal dunes (Hesse, 2010), up to several tens of kilometres long and approximately 6 m in height (Figure 3). Inter-dune spacing is approximately 500 m and dunes can

be greater than several hundred metres in width. Blowout features are present on the crests of some dunes, but most are currently stabilized by vegetation. The eroded remnants of a presumably older northeast trending dune set locally form closed depressions with the southeast trending dune set.

The land surface in the vicinity of the Petermann rupture slopes gently south to southwest and is characterized by sparse evidence for channelized drainage. Broad, shallow paleo-channels draining towards the southwest are truncated by the northwest-trending dune set, forming strings of playas in interdune regions (Figures 1 and 3). Paleo-channel margins are locally framed by groundwater carbonate horizons, which form low escarpments, and in some cases have resulted in relief inversion (e.g., the ridge beneath the red arrow immediately south of profile line Z-Z' in Figure 3a). The paleo-drainage along which profile Y-Y' is constructed is illustrative of the landscape history. This drainage line is framed on the northwest side by a low escarpment developed in a groundwater carbonate horizon. The escarpment extends approximately 0.6 km northeast of the scarp and more than 3.5 km southwest (Figure 3b). This indicates that the relative base-level fall that triggered the incision leading to exhumation and exposure of the carbonate layer occurred more than 3.5 km to the southwest of the 2016 Petermann Ranges earthquake surface rupture, and so is unrelated to this event or prior events along the same line.

A comparison of pre- and post-earthquake topographic profiles from within this paleo-channel (profile Y-Y'), and two shield plain locations (profiles X-X' and Z-Z') supports this observation. Nor is there evidence in the topography or dune systems to suggest incising drainage or migrating nick-points across the region of hanging-wall uplift of the modern rupture. In general, there is no indication of pre-existing tectonic relief along the line of the 2016 surface rupture (cf., Figure 3a,b).

3.2 | Trench logs

Trench 1 was excavated across the Petermann Ranges earthquake surface rupture within a playa occupying the axis of the shallow paleovalley (co-located with profile Y-Y' in Figure 3). The trench exposed coarsely layered to un-layered silty fine sand and fine sandy silt, with a minor to moderate component of medium sand. These clastic sediments are interpreted to reflect a combination of aeolian deposition and sheetwash from the side slopes and down the valley trend, and lacustrine deposition in the playa in which the trench was excavated. A massive (i.e., homogenous) powdery carbonate horizon is developed in these materials below 0.72 m depth, presumably as the result of groundwater flow through the paleovalley sediments (Krapf & Sheard, 2018; Magee, 2009).

Trench 1 shows a single main fault plane dipping 25° , with a minor splay as the fault reaches the surface. This fault offsets the top of the calcrete horizon by 0.25 m, consistent with RTK GPS measurements of vertical offset at this location (Attanayake et al., 2020; Gold et al., 2019). Minor fractures are observed in the hanging-wall sediments, extending to less than 50 cm depth and not always reaching the ground surface. Small nodules of calcrete are observed close to the rupture on the hanging-wall and may have been transported up-dip along the fault-plane.

Trench 2 was dug within an inter-dune location with bedrock outcrops on both hanging-wall and foot-wall (location is co-located with profile X-X' in Figure 3). Trench 2 also exposed a faulted calcrete horizon developed within aeolian and alluvial sediments. Medium sand is more abundant and silt less abundant in the clastic sediment profile in comparison to the profile in Trench 1. This is interpreted to reflect a primarily sheetwash origin with aeolian input. At 0.25 m depth a nodular pedogenic carbonate is developed with nodules up to 5 cm in diameter. This calcrete is dissimilar in texture to the massive calcrete exposed in Trench 1. While both calcrites are presumably related to groundwater flow, scattered bedrock outcrops in the vicinity of Trench 2 suggest that the nodular carbonate may be in part lithogenic.

Trench 2 has one main fault plane dipping 36° with a vertical offset of 0.4 m (consistent with RTK measurements) and 0.6 m along-fault (net-slip) measured across the top of the calcrete horizon. Offsets are measured relative to the calcrete horizon as rupture caused thickening and over-thrusting of the sediments on the foot-wall. Minor fractures are visible within the calcrete, with the same dip as the main fault. However due to the nodular and non-planar top of the calcrete horizon, it is not clear whether these fractures hosted offset. Many fractures are visible in the sediment on both hanging-wall and foot-wall orientated parallel and normal to the main fault. Many of these fractures do not reach the ground surface.

Vertical offsets measured across calcrete horizons exposed in both trenches are the same as RTK measurements across rupture at the surface (Attanayake et al., 2020; Gold et al., 2019), indicating aeolian/alluvium sediment and calcrete only preserve offsets relating to the 2016 Petermann earthquake.

3.3 | Optically stimulated luminescence burial age

All 24 measured aliquots exhibited good luminescence characteristics with bright signals dominated by the fast component (Figure 6a), exponential OSL signal increase as shown by the growth-response curve (Figure 6b), and all recycling ratios and infrared-depletion ratios consistent with unity (within 2 s). The resulting D_e distribution does not show asymmetry and has a low overdispersion of $\approx 12\%$ (Figure 6c) justifying the use of the CAM for paleodose and age calculation, and resulting in a burial age of 10.6 ± 0.4 ka (Table 1). This age is comparable to existing sedimentary and speleothem records that indicate active landscapes at this time, characterized by linear dune activity in the Tirari and Strzelecki deserts (Fitzsimmons et al., 2007), and alluvial sediment transport around the Flinders Ranges (Gliganic et al., 2014) under moist climatic conditions (Quigley, Horton, et al., 2010) dominated by summer rainfall (Singh & Luly, 1991). This age provides a minimum time interval for any prior ruptures on this fault, as trenching found no prior offset recorded in the dated sediments (Figure 4).

3.4 | Cosmogenic nuclide erosion rates

Bedrock erosion rates derived from time-dependent ^{10}Be production rate model LSDn (Lifton et al., 2014) range from 1.27 ± 0.10 to 2.57 ± 0.20 m Myr^{-1} with 7–12% relative uncertainties (Table 2, column LSDn in Table S1). Minimal (less than 1.5%) rate variation is observed

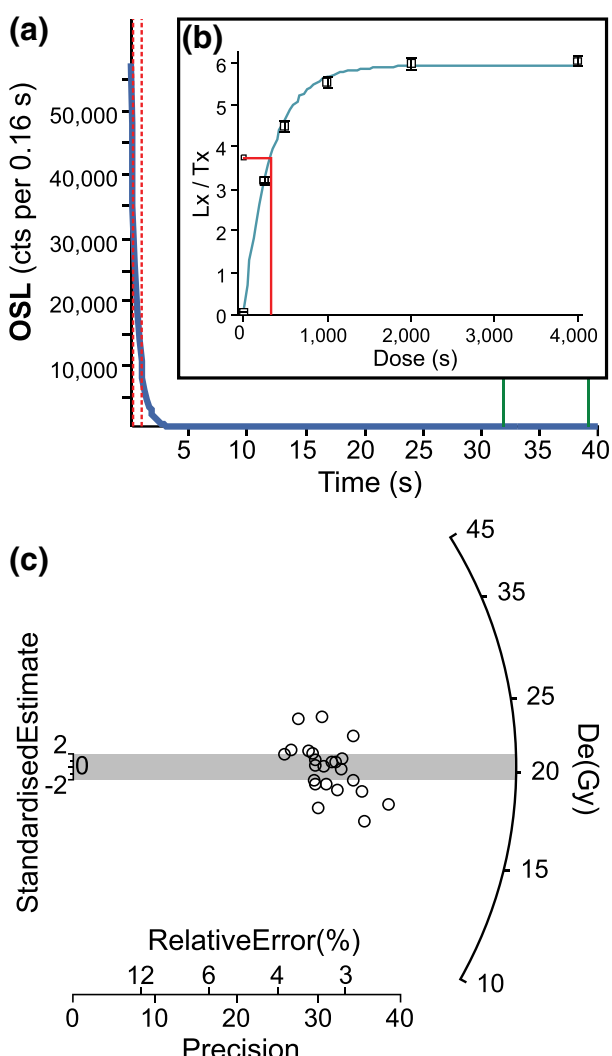


FIGURE 6 Luminescence properties of the OSL sample. (a) OSL signal decay curve with integration intervals for the natural signal (red) and background (green); (b) dose-response curve illustrating the growth of luminescence signal with laboratory dose and the determination of the equivalent dose (D_e) (red); (c) radial plot of the resulting D_e values [Color figure can be viewed at wileyonlinelibrary.com]

between these rates and those derived using the time-independent production model based on Stone (2000) and Lal (1991) (column St in Table S1). Erosion rates calculated with the production model based on Lifton et al., 2008 (column Lm in Table S1) are consistently 19% higher than the reported rates. Seven erosion rates (Samples A, D, E, F, G, H and J) are within 1σ error of each other and fall in the range 1.27–1.71 m Myr^{-1} . Likewise, the remaining three samples (Samples B, C and I) have overlapping error bars and fall in the range 2.21–2.57 m Myr^{-1} . The unweighted average and standard deviation of all Samples A–J is 1.75 ± 0.44 m Myr^{-1} .

As a comparison to these results, samples ($n = 2$) from low-lying exfoliating granite outcrops in the McDonnell Ranges (Figure 1) approximately 300 km northeast of this study site, yield erosion rates (2.2 ± 0.2 and 2.0 ± 0.2 m Myr^{-1} ; Heimsath et al., 2010) that are within error of the average rate established here (Figure 2). Similarly, exfoliating granite outcrop samples ($n = 6$) from the Devil's Marbles (Figure 1) approximately 650 km northeast of this study site yield an average erosion rate of 1.6 ± 0.2 m Myr^{-1} (Bierman & Caffee, 2002; Portenga & Bierman, 2011).

We cannot identify any correlation between erosion rate and (i) proximity of the sample to the surface rupture zone, (ii) samples located on the hanging-wall versus foot-wall, or (iii) samples in the epicentral area versus far-field regions. We also find no correlation between erosion rate and height of the sample above the sandplain. This lack of spatially variable erosion rates is explored in more detail in the Discussion section (Section 4.3).

Equation (1): $1 \text{ m} - x \text{ Myr} * (\text{Er}_{\max} - \text{Er}_{\min \text{ [or avg]}})$ provides an estimate of how long bedrock offsets related to 1 m coseismic displacement will reside in the landscape, with 0.4–0.6 m of hanging-wall displacement remaining (relative to the footwall) after 0.5 Myr, and 0.0–0.2 m within 1 Myr (Figure 5b). Application of this approach suggests the Petermann scarp (with vertical displacements of 0.1 to 1 m) and associated uplifted topography could be erosionally removed within 0.5–1 Myr (Figure 5b). While this estimate is highly uncertain, and subject to the assumptions made earlier, it provides a useful framework for understanding fault scarp residence times in this slowly eroding landscape. This framework is explored in more detail in the Discussion section (Section 4.4).

Equation (2) Λ / ε provides an approximate value for the timescale over which our assumptions of steady-state erosion and infinite exposure are applicable (and hence over which our erosion rates might be reasonably extrapolated). This equation is solved by equating Λ with the attenuation length of the mechanism that dominates production near the surface. For ^{10}Be , that mechanism is spallation by fast neutrons, for which $\Lambda \approx 150 \text{ g cm}^{-2}/2.7 \text{ g cm}^{-3} \approx 55 \text{ cm}$ (Gosse & Phillips, 2001). Applying Λ / ε for our highest (2.57 m Myr^{-1}) and lowest (1.27 m Myr^{-1}) erosion rates, suggests our calculated erosion rate average is representative over approximately the last 0.2–0.4 Myr. Extending our erosion rate results past this time-range (such as in our 0.5–1 Myr estimate for time required to erode the Petermann scarp) introduces large epistemic uncertainties into our interpretations. This is explored in more detail in the Discussion section (Section 4.5).

4 | DISCUSSION

4.1 | Erosion rate variations

We observe a bimodality in our erosion rates with ranges of 1.27 to 1.71 m Myr^{-1} and 2.21 to 2.57 m Myr^{-1} . This may be attributed to outcrop scale differences in erodibility (e.g., variable lithology and fracture density) and/or erosion (e.g., variable exposure to erosive forces such as wind and water). Alternatively (or additionally), the cohort of higher erosion rates could relate to different spatial and temporal scales of episodic erosion (Figure 7) via periodic or stochastic removal of previously overlying rock fragments of unknown thickness, but with a minimum probable thickness less than 30–50 cm in order to generate the observed variability (Small et al., 1997).

Differences in erosional processes (e.g., wind vs. water) are unlikely at the scale considered since no relationship between site elevation and erosion rate, nor field evidence for variations in fluvial or aeolian erosional processes, were found. However, at many sample sites we identified proximal evidence for *in situ* exfoliating rock sheets and eroding boulders greater than 30 to 50 cm thick, as well as eroded rock debris near sampled outcrops with similar properties (Figures 2 and 7).

Our favoured hypothesis is that bedrock in the study area erodes via a combination of (i) exfoliation of thin (thickness less than 5 to 10 cm) sheets that can be approximated by the steady-state erosion rate assumption (Lal, 1991; Figure 7) and (ii) episodic, and probably stochastic, erosion of thicker (greater than 30 to 50 cm) overlying rock fragments (i.e., boulders, Figure 7) that locally increase the apparent erosion rate (Small et al., 1997). We argue that an unresolved combination of these processes is responsible for most of the variability in the 10 erosion rates determined from *in situ* produced ^{10}Be .

4.2 | Coseismic erosion during the Petermann earthquake and implications for cosmogenic ^{10}Be concentrations

Previous work on Australian faults with Quaternary offsets in the similarly arid Flinders Ranges found that bedrock and sediment proximal to the faults recorded increases in the mean and standard deviation of ^{10}Be erosion rates (Quigley et al., 2007). This work suggested that earthquake-induced erosion rate perturbations could persist above background (pre-seismic) rates for greater than 30 kyr within the arid Australian landscape. This hypothesis suggested multiple processes could lead to enhanced delivery of material low in ^{10}Be to the sampled catchments, increasing the apparent erosion rate. These include: seismically-triggered landslides (e.g., Niemi et al., 2005); seismic shaking and *in situ* rock fracturing (e.g., Quigley et al., 2016); and steepening of stream profiles and catchment flanks via upstream propagation of earthquake-induced knickpoints (Wobus et al., 2005). These mechanisms could influence ^{10}Be erosion rates over sustained ($> 10^3$ to 10^6) timescales, dependent upon conditions including the nature of the perturbation relative to background erosion rates, lithologies, topography, vegetation, rates of natural and anthropogenic surface processes, landscape interactions, and climate-weather variability. Quigley, Clark and Sandiford (2010) proposed a positive correlation between regional seismic strain rate and average ^{10}Be erosion rates across the Australian continent. Within this context, it is valuable to consider whether coseismic erosion induced by the 2016 Petermann earthquake, in this significantly more subdued landscape relative to those studied elsewhere in Australia, could be expected to perturb bedrock ^{10}Be concentrations in a manner consistent with that proposed by Quigley, Horton, et al. (2010) and Quigley, Clark and Sandiford (2010).

Episodic removal of rock fragments of different thicknesses affects steady-state erosion rate estimates differently depending on the rate of erosion. Lines of equal relative uncertainty (i.e., the ratio of uncertainty to erosion rate) are shown on Figure 5(a) (adapted from figure 6, Small et al., 1997). These lines vary depending on rock fragment thickness and mean erosion rate (Small et al., 1997). For example, for very low erosion rates (e.g., $< 1.0 \text{ m Myr}^{-1}$) 10 cm thick rock removal results in high variability around the sample mean (relative uncertainty $\approx 7\text{--}20\%$). For high erosion rates (e.g., $> 10 \text{ m Myr}^{-1}$) the erosion rate recovers quickly from removal of 10 cm and their relative uncertainty is lower ($\approx 5\%$).

The thickness range of exfoliated rock sheets/fragments (2–5 cm) displaced in the Petermann earthquake (King et al., 2018) is plotted against our ^{10}Be erosion rates ($1.27\text{--}2.57 \text{ m Myr}^{-1}$; Table 2) in Box (i) of Figure 5(a). Box (i) crosses the lines of equally relative uncertainty

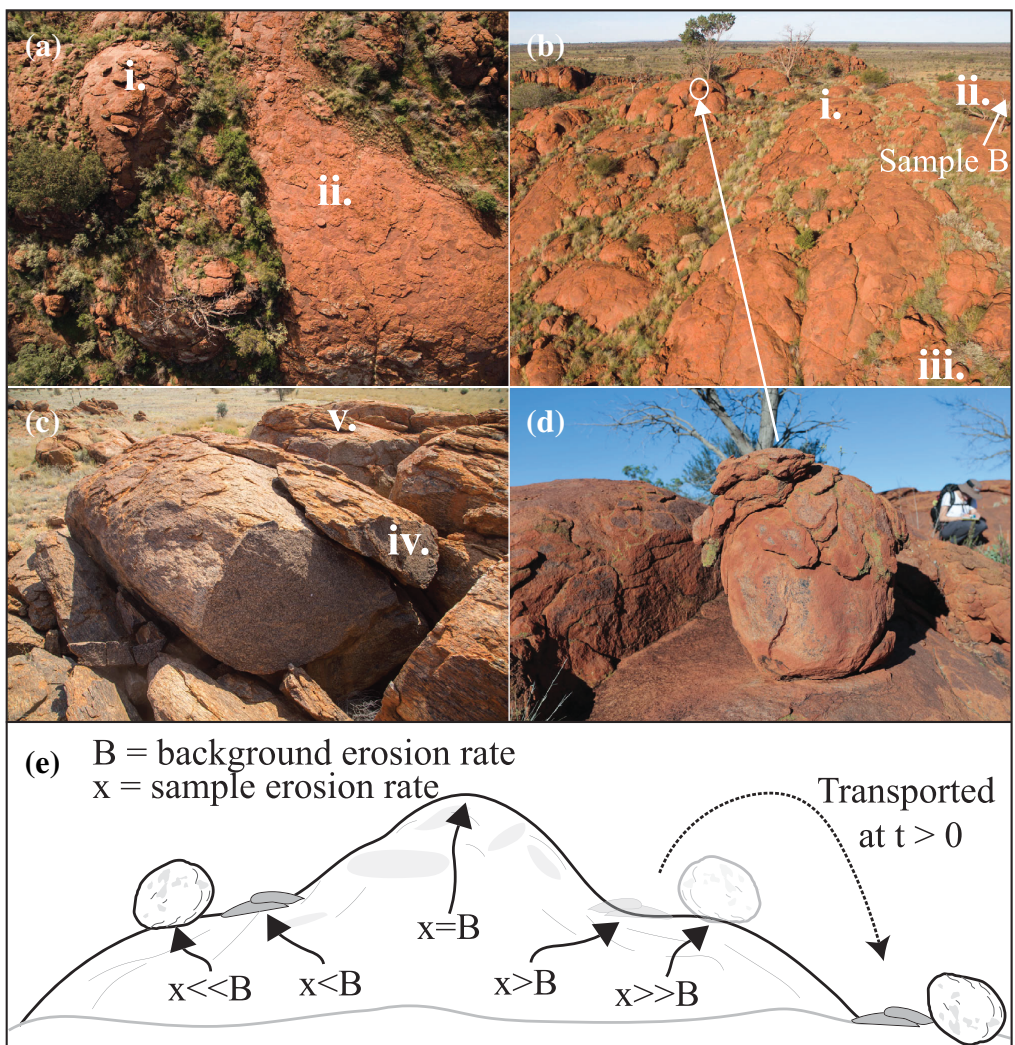


FIGURE 7 Erosional style variability in bedrock outcrops adjacent to the 2016 Petermann surface rupture which may locally perturb ^{10}Be erosion rates (a) 2–6 m high bedrock outcrop with sub-horizontal outcrop peak showing (i) region with 2–5 cm thick exfoliation sheets loosely- to un-attached but still resting on bedrock (ii) region where older exfoliation sheets have been removed (−25.583, 129.792; WGS84); (b) the side and top of 8 to 10 m high bedrock outcrop (location of Sample B with highest recorded erosion rate; Table 2) showing variable exfoliation sheet removal as with (a) (i) and (ii), and rounded blocks both in situ (e.g., (d)) and (iii) at transported to down-slope locations (−25.627, 129.746; WGS84); (c) less than 3 m high bedrock outcrop (location of Sample I with second highest recorded erosion rate; Table 2) showing (iv) 2–20 cm thick block of bedrock partly transported from original bedrock location and (v) 5–10 cm thick exfoliation sheet in situ on top of outcrop (−25.523, 129.636; WGS84); (d) image of in situ rounded boulder visible in (b) of 20 to 30 cm thickness (−25.627, 129.746; WGS84); (e) schematic representation on how episodic removal of exfoliation sheets and larger boulders may effect erosion rate, x , relative to background erosion rate, B [Color figure can be viewed at wileyonlinelibrary.com]

from ≈ 1.5 to 3%. This indicates that the potential range of new erosion rates following removal of 2 to 5 cm sheet is low, even if sampling prior to or after an exfoliation event (assuming steady-state erosion). Box (ii) of Figure 5(a) shows the range of our reported relative uncertainties (7.5–11.8%; Table 2). Box (iii) of Figure 5(a) represents the thicknesses of rock fragments (greater than 13 to 15 cm, labelled *(iv) on x axis) that would be required to induce 1σ variations from steady-state erosion.

Displaced rocks with thicknesses exceeding this 13 to 15 cm threshold value were only very rarely observed (1×10^{-4} % of area of observed outcrops) on steep bedrock faces (i.e., rockfalls) and never from flat-lying bedrock surfaces (King et al., 2018). Coseismic rock fragments displaced from sub-horizontal surfaces in the Petermann earthquake are thus of insufficient thickness (< 13 cm) to perturb ^{10}Be concentrations in the underlying bedrock, and no ^{10}Be evidence

for coseismic processes on these surfaces will be evident. While isolated occurrences of seismically triggered rockfalls are of sufficient depth to perturb ^{10}Be concentrations, these outcrops collectively account for << 0.1% of the total outcrop area in the epicentral region. The utility of these surfaces to constrain past rupture behaviours on the Petermann fault via ^{10}Be analysis is therefore limited without independent evidence (e.g., Quigley et al., 2007).

While the thicknesses of rocks displaced by the Petermann earthquake may not produce immediate long-term perturbation of erosion rates, coseismic uplift and *in situ* rock fracturing could still influence ^{10}Be concentrations over longer timescales. Coseismic changes in topography and rock mass strength are likely to significantly perturb surface processes by locally increasing erosion rates on the uplifted (and more strongly fractured) hanging wall of the Petermann fault. This would result in a spatially distinct ^{10}Be cosmogenic signal close

to the surface rupture relative to regional rates, and in hanging-wall versus foot-wall rates (see next section). We hypothesize that spatially variable erosion rates resulting from prior ruptures of this fault may persist over a longer time range than fault-related offsets analogous to the 2016 event (i.e., < 1 m).

4.3 | Expected longevity of the Petermann earthquake scarp and implications for active fault recognition

The Petermann earthquake fault scarp traverses both bedrock and sedimentary landscape elements (King et al., 2018). Sheetwash and channel-related alluvial erosional processes were observed (King et al., 2018) to erode the scarp more rapidly than adjacent surfaces due to the enhanced topographic slope at the scarp (Colman & Watson, 1983; McCalpin, 2009). The erodibility and rate of migration of knickpoints into the uplifted topography may be further enhanced by coseismic fracturing and fissuring of hanging-wall outcrops (Hsu & Pelletier, 2004; McCalpin, 2009). Within 1 to 2 weeks of the Petermann earthquake, large storms removed and/or obscured fine detail in scarp-related structural features and smoothed scarps in the unconsolidated surface sediment (King et al., 2018); similar erosional processes are expected to continue to erode and obscure the fault scarp. Small displacements at fault scarp tips and displacements in unconsolidated sediment may thus have short residence times in this landscape before they are unrecognizable. The length of time in which a fault scarp is recognizable in the landscape has implications for the production and completeness of Quaternary-active fault databases (Clark, 2012) used in seismic hazard analysis, particularly in areas of low to geodetically unresolvable strain rates. Estimating the landscape residence time of earthquake scarps may also help to constrain Mmax and moment rate estimates across similar crustal regions (e.g., Leonard & Clark, 2011).

Equation (1) suggests the Petermann scarp (with vertical displacements of 0.1 to 1 m) and associated uplifted topography could be erosionally removed within 0.5–1 Myr (Figure 5b). While this estimate is highly uncertain, and subject to the assumptions made earlier, it provides a useful framework for understanding fault scarp residence times in this slowly eroding landscape.

4.4 | Rupture history of the Petermann fault

The alluvial and aeolian sediments which overlie the calcrete layer in Trench 1 are only offset by the 2016 earthquake rupture (Table 1, Figure 4). The 10.6 ± 0.4 ka OSL age of these sediments indicates that no prior Holocene ruptures have occurred on the excavated trace of the Petermann faults. Examination of Worldview-1 data (Figure 3) revealed no geomorphic or visual evidence for features that could be interpreted as analogous predecessors of the fault scarp and uplift zone created in the 2016 Petermann earthquake. Approximately 0.5 to 1 Myr of differential erosion at the minima (footwall) and maxima (hanging wall) erosion rate estimates would be required to bevel the contemporary fault scarp and uplifted hanging wall to the pre-earthquake topography. By inference, any pre-2016 fault-related topography is likely to have required a similar time period for removal.

The Petermann earthquake therefore appears to be the first surface-rupturing earthquake on this fault, or any other potential proximal faults in the epicentral region, in the last 10 ka to 1 Myr or longer.

We note that as the time over which we extrapolate our results increases, the epistemic uncertainty associated with data limitations and assumptions increases. It is therefore difficult to speculate on the pre-0.5 to 1 Ma earthquake history of the Petermann fault. We consider it equally plausible that the 2016 Petermann earthquake was the first ever ground surface rupturing earthquake on this fault, or that prior analogous earthquake(s) occurred > 0.5 to 1 Myr ago. The Petermann fault is favourably orientated for rupture in Australia's active intraplate stress-field which has been extant since at least the late Miocene (i.e., commencement of 'neotectonic' deformation at ca. 5–10 Ma; Hillis et al., 2008; Sandiford et al., 2004) and possibly much longer (e.g., Eocene; Preiss, 2019). The maximum age interval over which our inter-seismic period estimate is applicable (1 Ma) thus allows for the potential of prior earthquakes on the Petermann fault within the active intraplate stress-field. We are unable to further evaluate the potential for a penultimate earthquake(s) on the Petermann fault with available evidence.

Evidence from a potentially analogous surface-rupturing fault (the rupture source for the 1986 Marryat Creek earthquake) suggests it was the first brittle offset of bedrock fabrics since the Precambrian (Machette et al., 1993). It is possible that the 2016 Petermann earthquake was similarly the first ever surface-rupturing earthquake on the Petermann fault. Further trenching aimed at observing the elevation of subsurface bedrock on both sides the Petermann fault may constrain this hypothesis, though we note that the remote nature of the event provides significant financial and logistical challenges for such an endeavour.

4.5 | Implications for seismic hazard modelling

Conceptually, for the purposes of probabilistic seismic hazard assessment, a fault source is a seismogenic fault that has produced earthquakes in the past and can be expected to continue doing so (Musson, 2012). Long-term slip rates are a key component of fault source input data for seismic hazard modelling (e.g., Allen et al., 2020; Stirling et al., 2012). While the Petermann fault demonstrably represents a historical seismic source, the lack of a determinable slip-rate challenges its inclusion in such models. If moderate to large earthquakes are assumed to recur on the faults that comprise the 2016 Petermann rupture, the long-term average uplift rate (i.e., the vertical component of the slip rate) is limited by our very low regional bedrock erosion rate determinations of ~ 1 to 3 m Myr $^{-1}$ (Table 2). This low rate is unlikely to contribute significantly to ground-motion hazard for return periods that may affect ordinary-use structures (e.g., 475 or 2475 years) (Allen, Griffin, et al., 2018).

More broadly there is no compelling evidence for prior Quaternary events on any of the faults that have hosted Australia's 11 historical surface rupturing earthquakes (Clark et al., 2020; King et al., 2019). These faults have either hosted 'one-off' ruptures or have interseismic periods extending beyond 10^5 to 10^6 years (this study; Clark et al., 2020; King et al., 2019).

In contrast, paleoseismic investigations of pre-historic fault scarps in the Precambrian SCR of Australia have identified recurrence of

large Quaternary earthquakes that enable the estimation of slip-rates. These include the Hyden fault (Clark et al., 2008), Lort River fault (Estrada et al., 2006; Thom, 1971), Dumbleyung fault (Estrada et al., 2006) and Mount Narreyer fault (Whitney et al., 2016; Williams, 1978). Recurrence has also been demonstrated on faults in the younger (Phanerozoic) regions of Australia (e.g., Clark et al., 2012; Clark, McPherson, et al., 2017; Quigley, Clark, & Sandiford, 2010).

In both of these settings there is evidence that large earthquake occurrence on some faults might be temporally-clustered (e.g., Crone et al., 1997; Clark, McPherson, et al., 2017). The current lack of defensible mechanism to explain these observations (e.g., Calais et al., 2016) introduces significant uncertainty when such faults are included as sources into seismic hazard models (Clark & Edwards, 2018; Clark et al., 2020).

Seismic hazard models commonly account for the potential for unmapped active faults, and for ‘one-off’ ruptures, by permitting moderate-to-large magnitude (i.e., M_w 5.0–7.0) ‘distributed earthquakes’ to occur anywhere (e.g., Stirling et al., 2008). These ensemble models of seismic hazard weight both fault source-based versus distributed seismicity logic tree branches (Allen, Griffin, et al., 2018, 2020; Clark et al., 2016; Griffin et al., 2018). Multi-methods studies such as ours are necessary to parameterize fault source models, to provide an evidential base for deciding the balance of weighting between logic tree branches for specific tectonic environments within low-strain rate regions (e.g., Clark et al., 2020).

Thus while many of the faults discussed in this article are very remote and represent a low risk to Australia’s spatially concentrated population, the knowledge gained in studying the behaviour of such faults contributes directly to the development of more robust and defensible seismic hazard models, and thereby benefits populated centres. Moreover, insight gained through studies of Australian surface rupturing faults and paleoseismic scarps may be applied to analogous low-strain rate regions globally (e.g., Crone et al., 1997, 2003).

5 | CONCLUSIONS

This article presents a multi-methods approach to quantifying landscape evolution rates in the near-fault region of the 2016 M_w 6.1 Petermann earthquake to understand the prior rupture history of this fault and to expand the time-range and confidence over which paleoseismic studies may be undertaken. Interpretation of results from landscape analysis (using pre- and post-earthquake satellite imagery), OSL dating, and cosmogenic ^{10}Be nuclide erosion rate sampling across the near- and far-field of the modern rupture area show an absence of evidence for penultimate rupture. We estimate that the Petermann scarp and associated hanging-wall uplift could be erosionally removed in 0.5–1 Myr. This suggests the Petermann earthquake may be the first surface-rupturing event on this fault in the last 10 ka to 1 Myr or longer. Extrapolating our assumptions and single nuclide erosion rates across timeframes > 0.4 Ma introduces large epistemic uncertainties. We therefore cannot definitively say whether the 2016 event was the first surface rupturing event on this fault, or that this fault has a > 1 Myr interseismic period. Either option negates the derivation of a meaningful long-term slip-rate or recurrence model for this fault, which are key inputs for fault sources in seismic hazard models. We suggest that the occurrence of future analogous surface-rupturing

earthquakes on unidentified faults may be addressed by including distributed seismicity components in seismic hazard.

DATA AND RESOURCES

The DEMs used in this article are subject to third party restrictions and were originally produced by Gold et al. (2019) DOI: 10.1029/2019GL084926. Restrictions apply to the availability of these data. All cosmogenic nuclide and OSL sample data are provided in Table 1 and/or the Supporting Information. Additional trench images are provided in Supporting Information, with more available upon request from the author.

ACKNOWLEDGEMENTS

The authors acknowledge the Antakirinja, Yankunytjatjara, and Pitjantjatjara people of the Western Desert and APY lands in South Australia/Northern Territory as the traditional custodians of the land on which the Petermann earthquake occurred, and where the data described in this article were collected. This research was funded by the Australian Research Council to M. Quigley through Discovery Grant #DP170103350. T. King received funding through the Australian Government Research Training Programme Scholarship and support from the David Hay Postgraduate Writing-Up Award (University of Melbourne). T. King also receives funding from COMET, the NERC Centre for the Observation and Modelling of Earthquakes, Volcanoes and Tectonics, a partnership between UK Universities and the British Geological Survey. D. Clark publishes with the permission of the Chief Executive Officer of Geoscience Australia. The authors thank Schirin Sellmann for assistance in OSL sample processing. The authors thank Ross Whitmore, an anonymous reviewer, the editors, and Paula Figueiredo for feedback which helped improve this manuscript.

DECLARATION OF INTEREST STATEMENT

The authors declare no potential conflicts of interest.

ORCID

- Tamarah Rosellen King  <https://orcid.org/0000-0002-9654-2917>
- Mark Quigley  <https://orcid.org/0000-0002-4430-4212>
- Dan Clark  <https://orcid.org/0000-0001-5387-4404>
- Jan-Hendrik May  <https://orcid.org/0000-0001-5758-9459>

REFERENCES

- Adamiec, G. & Aitken, M. (1998) Dose rate conversion factors. *Ancient TL*, 16, 37–50.
- Aitken, M.J. (1985) *Thermoluminescence dating*. London: Academic Press.
- Allen, T., Griffin, J., Leonard, M., Clark, D. & Ghasemi, H. (2018) *The 2018 National Seismic Hazard Assessment: Model overview* (GA Record 2018/27). Canberra, ACT: Geoscience Australia, Commonwealth of Australia.
- Allen, T., Griffin, J., Leonard, M., Clark, D. & Ghasemi, H. (2020) *The 2018 National Seismic Hazard Assessment of Australia: Quantifying hazard changes and model uncertainties*. *Earthquake Spectra*, 36(1_suppl), 1–37. <https://doi.org/10.1177/8755293019900777>
- Allen, T., Leonard, M., Ghasemi, H. & Gibson, G. (2018) *The 2018 National Seismic Hazard Assessment: Earthquake epicentre catalogue* (GA Record 2018/30). Canberra, ACT: Geoscience Australia, Commonwealth of Australia.
- Amos, C.B., Lapwood, J.J., Nobes, D.C., Burbank, D.W., Rieser, U. & Wade, A. (2011) Palaeoseismic constraints on Holocene surface

- ruptures along the Ostler Fault, southern New Zealand. *New Zealand Journal of Geology and Geophysics*, 54(4), 367–378. <https://doi.org/10.1080/00288306.2011.601746>
- ANCOLD (Australian National Committee on Large Dams). (2019) Guidelines for Design of Dams and Appurtenant Structures for Earthquake. Hobart, TAS: ANCOLD.
- Attanayake, J., King, T.R., Quigley, M.C., Gibson, G., Clark, D., Jones, A. & Sandiford, M. (2020) Rupture Characteristics and the Structural Control of the 2016 Mwp 6.1 Intraplate Earthquake in the Petermann Ranges, Australia. *Bulletin of the Seismological Society of America*, 110(3), 1037–1045. <https://doi.org/10.1785/0120190266>
- Atwater, B.F., Tuttle, M.P., Schweig, E.S., Rubin, C.M., Yamaguchi, D.K. & Hemphill-Haley, E. (2003) Earthquake recurrence inferred from paleoseismology. *Developments in Quaternary Science*, 1, 331–350. [https://doi.org/10.1016/S1571-0866\(03\)01015-7](https://doi.org/10.1016/S1571-0866(03)01015-7)
- Balco, G., Stone, J.O., Lifton, N.A. & Dunai, T.J. (2008) A complete and easily accessible means of calculating surface exposure ages or erosion rates from ^{10}Be and ^{26}Al measurements. *Quaternary Geochronology*, 3(3), 174–195. <https://doi.org/10.1016/j.quageo.2007.12.001>
- Bell, J.G., Kilgour, P.L., English, P.M., Woodgate, M.F., Lewis, S.J. & Wischusen, J.D.H. (2012) WASANT Palaeovalley Map - Distribution of Palaeovalleys in Arid and Semi-arid WA-SA-NT. Canberra, ACT: Geoscience Australia.
- Bierman, P.R. & Caffee, M.W. (2002) Cosmogenic exposure and erosion history of Australian bedrock landforms. *Bulletin of the Geological Society of America*, 114(7), 787–803. [https://doi.org/10.1130/0016-7606\(2002\)114<0787:CEAEHO>2.0.CO;2](https://doi.org/10.1130/0016-7606(2002)114<0787:CEAEHO>2.0.CO;2)
- Braun, J., Burbidge, D.R., Gesto, F.N., Sandiford, M., Gleadow, A.J.W., Kohn, B.P. & Cummins, P.R. (2009) Constraints on the current rate of deformation and surface uplift of the Australian continent from a new seismic database and low-T thermochronological data. *Australian Journal of Earth Sciences*, 56(2), 99–110. <https://doi.org/10.1080/08120090802546977>
- Calais, E., Camelbeeck, T., Stein, S., Liu, M. & Craig, T.J. (2016) A new paradigm for large earthquakes in stable continental plate interiors. *Geophysical Research Letters*, 43(20), 10,621–10,637. <https://doi.org/10.1002/2016GL070815>
- Calais, E., Mattioli, G., DeMets, C., Nocquet, J.-M., Stein, S., Newman, A. & Rydelek, P. (2005) Tectonic strain in plate interiors? *Nature*, 438, E9–E10. <https://doi.org/10.1038/nature04428> [online] Available from: <http://www.nature.com/articles/nature04428>
- Clark, D. (2012) Neotectonic Features Database. Canberra, ACT: Geoscience Australia, Commonwealth of Australia.
- Clark, D. (2018) What have we learned in the 50 years since the 1968 Meckering earthquake?. Canberra, ACT: Geoscience Australia, Commonwealth of Australia.
- Clark, D., Cupper, M., Sandiford, M. & Kiernan, K. (2011) Style and timing of late Quaternary faulting on the Lake Edgar fault, southwest Tasmania, Australia: Implications for hazard assessment in intracratonic areas. In: Audemard, M.F.A., Michetti, A.M. & McCalpin, J.P. (Eds.) *Geological Criteria for Evaluating Seismicity Revisited: Forty Years of Paleoseismic Investigations and the Natural Record of Past Earthquakes: Geological Society of America Special Paper 479*. Boulder, CO: The Geological Society of America, pp. 109–131.
- Clark, D., Dentith, M., Wyrwoll, K.-H., Yanchou, L., Dent, V.F. & Featherstone, W.E. (2008) The Hyden fault scarp, Western Australia: paleoseismic evidence for repeated Quaternary displacement in an intracratonic setting. *Australian Journal of Earth Sciences*, 55(3), 379–395. <https://doi.org/10.1080/08120090701769498>
- Clark, D. & Edwards, M. (2018) 50th anniversary of the 14th October 1968 Mw 6.5 (Ms 6.8) Meckering earthquake (GA Record 2018/39). Canberra, ACT: Geoscience Australia, Commonwealth of Australia.
- Clark, D., Griffin, J., Stirling, M. & Davies, G. (2017) Towards modelling the hazard relating to episodically slipping faults in slowly deforming regions [online] Available from: http://www.earthquakegeology.com/materials/proceedings/2017_Blenheim.pdf
- Clark, D., Leonard, M., Griffin, J., Stirling, M.W. & Volti, T. (2016) Incorporating fault sources into the Australian National Seismic Hazard Assessment (NSHA) 2018 [online] Available from: <http://creativecommons.org/licenses/by/4.0/legalcode>
- Clark, D. & McPherson, A. (2013) A tale of two seisms: Ernabella 23/03/2012 (Mw5.4) and Mulga Park 09/06/2013 (Mw 5.6), Newsletter. Melbourne, VIC: Australian Earthquake Engineering Society.
- Clark, D., McPherson, A., Allen, T. & De Kool, M. (2014) Coseismic surface deformation caused by the 23 March 2012 Mw 5.4 Ernabella (Pukatja) earthquake, central Australia: Implications for fault scaling relations in cratonic settings. *Bulletin of the Seismological Society of America*, 104(1), 24–39. <https://doi.org/10.1785/0120120361>
- Clark, D., McPherson, A., Cupper, M., Collins, C.D.N. & Nelson, G. (2017) The Cadell fault, southeastern australia: A record of temporally clustered morphogenic seismicity in a low-strain intraplate region. *Geological Society Special Publication*, 432(1), 163–185. <https://doi.org/10.1144/SP432.2>
- Clark, D., McPherson, A. & Van Dissen, R.J. (2012) Long-term behaviour of Australian stable continental region (SCR) faults. *Tectonophysics*, 566–567, 1–30. <https://doi.org/10.1016/j.tecto.2012.07.004> [online] Available from: <http://linkinghub.elsevier.com/retrieve/pii/S0040195112004076>
- Clark, D.J., Brennan, S., Brenn, G., Garthwaite, M.C., Dimech, J., Allen, T. I. & Standen, S. (2020) Surface deformation relating to the 2018 Lake Muir earthquake sequence, southwest Western Australia: New insight into stable continental region earthquakes. *Solid Earth*, 11(2), 691–717. <https://doi.org/10.5194/se-11-691-2020>
- Colman, S.M. & Watson, K. (1983) Ages estimated from a diffusion equation model for scarp degradation. *Science*, 221, 263–265.
- Coppersmith, K.J. & Youngs, R.R. (2000) Data needs for probabilistic fault displacement hazard analysis. *Journal of Geodynamics*, 29(3–5), 329–343. [https://doi.org/10.1016/S0264-3707\(99\)00047-2](https://doi.org/10.1016/S0264-3707(99)00047-2)
- Craig, T.J., Calais, E., Fleitout, L., Bollinger, L. & Scotti, O. (2016) Evidence for the release of long-term tectonic strain stored in continental interiors through intraplate earthquakes. *Geophysical Research Letters*, 43(13), 6826–6836. <https://doi.org/10.1002/2016GL069359>
- Crone, A.J., De Martini, P.M., Machette, M.N., Okumura, K. & Prescott, J.R. (2003) Paleoseismicity of two historically quiescent faults in Australia: Implications for fault behavior in stable continental regions. *Bulletin of the Seismological Society of America*, 93, 1913–1934. <https://doi.org/10.1785/0120000094> [online] Available from: <http://www.bssaonline.org/content/93/5/1913.abstract>
- Crone, A.J., Machette, M.N. & Bowman, J.R. (1992) *Geologic Investigations of the 1988 Tennant Creek, Australia, Earthquakes – Implications for Paleoseismicity in the Stable Continental Regions (USGS Bulletin 2032-A)*. Washington, DC: US Geological Survey.
- Crone, A.J., Machette, M.N. & Bowman, J.R. (1997) Episodic nature of earthquake activity in stable continental regions revealed by paleoseismicity studies of Australian and North American quaternary faults. *Australian Journal of Earth Sciences*, 44, 203–214. <https://doi.org/10.1080/08120099708728304> [online] Available from: <http://www.tandfonline.com/doi/abs/10.1080/08120099708728304>
- Dixon, T.H., Norabuena, E. & Hotaling, L. (2003) Paleoseismology and global positioning system: Earthquake-cycle effects and geodetic versus geologic fault slip rates in the eastern California shear zone. *Geology*, 31(1), 55–58. [https://doi.org/10.1130/0091-7613\(2003\)031<0055:PAGPSE>2.0.CO;2](https://doi.org/10.1130/0091-7613(2003)031<0055:PAGPSE>2.0.CO;2)
- Duller, G.A.T. (2003) Distinguishing quartz and feldspar in single grain luminescence measurements. *Radiation Measurements*, 37(2), 161–165. [https://doi.org/10.1016/S1350-4487\(02\)00170-1](https://doi.org/10.1016/S1350-4487(02)00170-1)
- Dunai, T.J. & Stuart, F.M. (2009) Reporting of cosmogenic nuclide data for exposure age and erosion rate determinations. *Quaternary Geochronology*, 4, 437–440. <https://doi.org/10.1016/j.quageo.2009.04.003>
- Edgoose, C.J., Scrimgeour, I.R. & Close, D.F. (2004) Geology of the Musgrave Block, Northern Territory (NTGS Report 15). In: Munson, T.J. (Ed.) Darwin, NT: Northern Territory Geological Survey.
- Ekström, G., Nettles, M. & Dziewoński, A.M. (2012) The global CMT project 2004–2010: Centroid-moment tensors for 13,017 earthquakes. *Physics of the Earth and Planetary Interiors*, 200–201, 1–9. <https://doi.org/10.1016/j.pepi.2012.04.002>
- Estrada B, Clark D, Wyrwoll K-H, Dentith M. 2006. Paleoseismic investigation of a recently identified Quaternary fault in Western Australia: the Dumbleyung Fault. Proceedings of the Australian Earthquake Engineering Society, Canberra ACT, November 2006: 189–194.

- Finch, E., Hardy, S. & Gawthorpe, R. (2003) Discrete-element modelling of contractional fault-propagation folding above rigid basement fault blocks. *Journal of Structural Geology*, 25(4), 515–528. [https://doi.org/10.1016/S0191-8141\(02\)00053-6](https://doi.org/10.1016/S0191-8141(02)00053-6)
- Fitzsimmons, K.E., Rhodes, E.J., Magee, J.W. & Barrows, T.T. (2007) The timing of linear dune activity in the Strzelecki and Tirari Deserts, Australia. *Quaternary Science Reviews*, 26(19–21), 2598–2616. <https://doi.org/10.1016/j.quascirev.2007.06.010>
- Frankel, K.L., Finkel, R.C. & Lewis, A.O. (2010) Terrestrial cosmogenic nuclide geochronology data reporting standards needed. *Eos*, 91(4), 31–32. <https://doi.org/10.1029/2010EO040003>
- Fujioka, T. & Chappell, J. (2010) History of Australian aridity: Chronology in the evolution of arid landscapes. *Geological Society Special Publication*, 346, 121–139. <https://doi.org/10.1144/SP346.8> [online] Available from: <http://sp.lyellcollection.org/lookup/doi/10.1144/SP346.8>
- Galbraith, R.F., Roberts, R.G., Laslett, G.M., Yoshida, H. & Olley, J.M. (1999) Optical dating of single and multiple grains of quartz from Jinmium rock shelter, northern Australia: Part I, experimental design and statistical models. *Archaeometry*, 41(2), 339–364. <https://doi.org/10.1111/j.1475-4754.1999.tb00987.x>
- Gliganic, L.A., Cohen, T.J., May, J.H., Jansen, J.D., Nanson, G.C., Dosseto, A. et al. (2014) Late-Holocene climatic variability indicated by three natural archives in arid southern Australia. *Holocene*, 24(1), 104–117. <https://doi.org/10.1177/0959683613515732>
- Gold, R.D., Briggs, R.W., Crone, A.J. & DuRoss, C.B. (2017) Refining fault slip rates using multiple displaced terrace risers—an example from the Honey Lake fault, NE California, USA. *Earth and Planetary Science Letters*, 477, 134–146. <https://doi.org/10.1016/j.epsl.2017.08.021>
- Gold, R.D., Clark, D., Barnhart, W.D., King, T.R., Quigley, M.C. & Briggs, R.W. (2019) Surface rupture and distributed deformation revealed by optical satellite imagery: The intraplate 2016 Mw 6.0 Petermann Ranges earthquake, Australia. *Geophysical Research Letters*, 46 (17–18), 10394–10403. <https://doi.org/10.1029/2019GL084926>
- Gosse, J.C. & Phillips, F.M. (2001) Terrestrial in situ cosmogenic nuclides: Theory and application. *Quaternary Science Reviews*, 20(14), 1475–1560. [https://doi.org/10.1016/S0277-3791\(00\)00171-2](https://doi.org/10.1016/S0277-3791(00)00171-2)
- Granger, D.E., Kirchner, J.W. & Finkel, R. (1996) Spatially averaged long-term erosion rates measured from in situ-produced cosmogenic nuclides in alluvial sediment. *Journal of Geology*, 104(3), 249–257. <https://doi.org/10.1086/629823>
- Griffin, J., Gerstenberger, M., Allen, T., Clark, D., Cummins, P., Cuthbertson, R. et al. (2018) Expert elicitation of model parameters for the 2018 National Seismic Hazard Assessment: Summary of workshop, methodology and outcomes (GA Record 2018/028). Canberra, ACT: Geoscience Australia.
- Hanks, T.C. (2000) The Age of Scarplike Landforms From Diffusion-Equation Analysis. In: Noller, J.S., Sowers, J.M. & Lettis, W.R. (Eds.) *Quaternary Geochronology: Methods and Applications*, Vol. 4. Washington, DC: American Geophysical Union 10.1029/RF004p0313.
- Hardy, S. & Finch, E. (2007) Mechanical stratigraphy and the transition from trishear to kink-band fault-propagation fold forms above blind basement thrust faults: A discrete-element study. *Marine and Petroleum Geology*, 24(2), 75–90. <https://doi.org/10.1016/j.marpetgeo.2006.09.001>
- Heimsath, A.M., Chappell, J. & Fifield, K. (2010) Eroding Australia: rates and processes from Bega Valley to Arnhem Land. *Geological Society, London, Special Publications*, 346(1), 225–241. <https://doi.org/10.1144/SP346.12>
- Hejrani, B. & Tkalcic, H. (2018) The 20 May 2016 Petermann Ranges earthquake: Centroid location, magnitude and focal mechanism from full waveform modelling. *Australian Journal of Earth Sciences*, 66, 37–45. <https://doi.org/10.1080/08120099.2018.1525783> [online] Available from: <http://www.tandfonline.com/action/journalInformation?journalCode=taje20>
- Hesse, P.P. (2010) The Australian desert dunefields: formation and evolution in an old, flat, dry continent. *Geological Society, London, Special Publications*, 346, 141–164. <https://doi.org/10.1144/SP346.9> [online] Available from: <http://sp.lyellcollection.org/lookup/doi/10.1144/SP346.9>
- Hillis, R.R., Sandiford, M., Reynolds, S.D. & Quigley, M.C. (2008) Present-day stresses, seismicity and Neogene-to-Recent tectonics of Australia's "passive" margins: intraplate deformation controlled by plate boundary forces. *Geological Society, London, Special Publications*, 306(1), 71–90. <https://doi.org/10.1144/SP306.3>
- Hornblow, S., Quigley, M., Nicol, A., Van Dissen, R. & Wang, N. (2014) Paleoseismology of the 2010 Mw 7.1 Darfield (Canterbury) earthquake source, Greendale Fault, New Zealand. *Tectonophysics*, 637, 178–190. <https://doi.org/10.1016/j.tecto.2014.10.004>
- Hsu, L. & Pelletier, J.D. (2004) Correlation and dating of Quaternary alluvial-fan surfaces using scarp diffusion. *Geomorphology*, 60(3–4), 319–335. <https://doi.org/10.1016/j.geomorph.2003.08.007>
- Johnston, A.C., Coppersmith, K.J. & Cornell, C.A. (1994) The earthquakes of stable continental regions. In: *Electric Power Research Institute Report TR-102261-VI*. Palo Alto, CA: EPRI Distribution Centre.
- Khajavi, N., Langridge, R.M., Quigley, M.C., Smart, C., Rezanejad, A. & Martín-González, F. (2016) Late Holocene rupture behavior and earthquake chronology on the Hope fault, New Zealand. *Bulletin of the Geological Society of America*, 128(11–12), 1736–1761. <https://doi.org/10.1130/B31199.1>
- King, T.R., Quigley, M.C. & Clark, D. (2018) Earthquake environmental effects produced by the Mw 6.1, 20th May 2016 Petermann earthquake, Australia. *Tectonophysics*, 747–748, 357–372. <https://doi.org/10.1016/j.tecto.2018.10.010>
- King, T.R., Quigley, M.C. & Clark, D. (2019) Surface-rupturing historical earthquakes in Australia and their environmental effects: new insights from re-analyses of observational data. *Geosciences*, 9(10), 1–34. <https://doi.org/10.3390/geosciences9100408>
- Krapf, C.B.E. & Sheard, M.J. (2018) *Regolith hand specimen atlas for South Australia*. Department of the Premier and. Adelaide, SA: Cabinet.
- Lal, D. (1991) Cosmic ray labeling of erosion surfaces: in situ nuclide production rates and erosion models. *Earth and Planetary Science Letters*, 104 (2–4), 424–439. [https://doi.org/10.1016/0012-821X\(91\)90220-C](https://doi.org/10.1016/0012-821X(91)90220-C)
- Leonard, M. (2008) One hundred years of earthquake recording in Australia. *Bulletin of the Seismological Society of America*, 98(3), 1458–1470. <https://doi.org/10.1785/0120050193>
- Leonard, M., Burbidge, D.R., Allen, T., Robinson, D.J., McPherson, A., Clark, D. & Collins, C. (2014) The challenges of probabilistic seismic-hazard assessment in stable continental interiors: An Australian example. *Bulletin of the Seismological Society of America*, 104(6), 3008–3028. <https://doi.org/10.1785/0120130248>
- Leonard, M. & Clark, D. (2011) A record of stable continental region earthquakes from Western Australia spanning the late Pleistocene: Insights for contemporary seismicity. *Earth and Planetary Science Letters*, 309, 207–212. <https://doi.org/10.1016/j.epsl.2011.06.035>
- Leonard, M., Schneider, J.F., Dhu, T. & Burbidge, D.R. (2007) Toward a better model of earthquake hazard in Australia. *The Geological Society of America Special Paper*, 425, 263–283. [https://doi.org/10.1130/2007.2425\(17\)](https://doi.org/10.1130/2007.2425(17))
- Lewis, J.D., Daetwyler, N.A., Bunting, J.A. & Montcrieff, J.S. (1981) *The Cadoux Earthquake (GSWA Report 11)*. Perth, WA: Geological Survey of Western Australia.
- Lifton, N., Sato, T. & Dunai, T.J. (2014) Scaling in situ cosmogenic nuclide production rates using analytical approximations to atmospheric cosmic-ray fluxes. *Earth and Planetary Science Letters*, 386, 149–160. <https://doi.org/10.1016/j.epsl.2013.10.052>
- Lifton, N.A., Smart, D.F. & Shea, M.A. (2008) Scaling time-integrated in situ cosmogenic nuclide production rates using a continuous geomagnetic model. *Earth and Planetary Science Letters*, 268(1–2), 190–201. <https://doi.org/10.1016/j.epsl.2008.01.021>
- Little, T.A., Van Dissen, R., Rieser, U., Smith, E.G.C. & Langridge, R.M. (2010) Coseismic strike slip at a point during the last four earthquakes on the Wellington fault near Wellington, New Zealand. *Journal of Geophysical Research: Solid Earth*, 115(B5), 1–22. <https://doi.org/10.1029/2009JB006589>
- Liu, M. & Stein, S. (2016) Mid-continental earthquakes: Spatiotemporal occurrences, causes, and hazards. *Earth-Science Reviews*, 162, 364–386. <https://doi.org/10.1016/j.earscirev.2016.09.016>
- Livio, F., Berlusconi, A., Zerbini, A., Trombino, L., Sileo, G., Michetti, A.M. et al. (2014) Progressive offset and surface deformation along a

- seismogenic blind thrust in the Po Plain foredeep (Southern Alps, northern Italy). *Journal of Geophysical Research: Solid Earth*, 119, 7701–7721. <https://doi.org/10.1002/2014JB011112>
- Livio, F., Kettermann, M., Reicherter, K. & Urai, J.L. (2019) Growth of bending-moment faults due to progressive folding: Insights from sandbox models and paleoseismological implications. *Geomorphology*, 326, 152–166. <https://doi.org/10.1016/j.geomorph.2018.02.012>
- Mabbutt, J.A. (1988) Australian desert landscapes. *GeoJournal*, 16(4), 355–369. <https://doi.org/10.1007/BF00214394>
- Machette, M.M.N., Crone, A.A.J. & Bowman, J.R. (1993) *Geologic investigations of the 1986 Marryat Creek, Australia, earthquake: implications for paleoseismicity in stable continental regions (USGS Bulletin 2032-B)*. Washington, DC: US Geological Survey.
- Machette, M.N. (2000) Active, capable, and potentially active faults – a paleoseismic perspective. *Journal of Geodynamics*, 29(3–5), 387–392. [https://doi.org/10.1016/S0264-3707\(99\)00060-5](https://doi.org/10.1016/S0264-3707(99)00060-5)
- Magee, J.W. (2009) *A Literature Review Palaeovalley Groundwater Resources in Arid and Semi-Arid Australia - A literature review*. Canberra, Australia: Geoscience Australia. <http://pid.geoscience.gov.au/dataset/ga/68542>
- McCalpin, J.P. (2009) Paleoseismology. In: *International Geophysics*, Vol. 95. San Diego, CA: Elsevier Science Publishing.
- Michael-Leiba, M., Love, D., McCue, K. & Gibson, G. (1994) The Uluru (Ayers Rock), Australia, Earthquake of 28 May 1989. *Bulletin of the Seismological Society of America*, 84, 209–214.
- Moss, R.E.S. & Ross, Z.E. (2011) Probabilistic fault displacement hazard analysis for reverse faults. *Bulletin of the Seismological Society of America*, 101(4), 1542–1553. <https://doi.org/10.1785/0120100248>
- Murray, A.S. & Wintle, A.G. (2000) Luminescence dating of quartz using an improved single-aliquot regenerative-dose protocol. *Radiation Measurements*, 32(1), 57–73. [https://doi.org/10.1016/S1350-4487\(99\)00253-X](https://doi.org/10.1016/S1350-4487(99)00253-X)
- Musson, R.M.W. (2012) Interpreting intraplate tectonics for seismic hazard: A UK historical perspective. *Journal of Seismology*, 16(2), 261–273. <https://doi.org/10.1007/s10950-011-9268-1>
- Nicol, A., Robinson, R., Van Dissen, R.J. & Harvison, A. (2016) Variability of recurrence interval and single-event slip for surface-rupturing earthquakes in New Zealand. *New Zealand Journal of Geology and Geophysics*, 59(1), 97–116. <https://doi.org/10.1080/00288306.2015.1127822>
- Niemi, N.A., Osokin, M., Burbank, D.W., Heimsath, A.M. & Gabet, E.J. (2005) Effects of bedrock landslides on cosmogenically determined erosion rates. *Earth and Planetary Science Letters*, 237(3–4), 480–498. <https://doi.org/10.1016/j.epsl.2005.07.009>
- Nishiizumi, K., Imamura, M., Caffee, M.W., Southon, J.R., Finkel, R.C. & McAninch, J. (2007) Absolute calibration of ^{10}Be AMS standards. *Nuclear Instruments and Methods in Physics Research, Section B: Beam Interactions with Materials and Atoms*, 258(2), 403–413. <https://doi.org/10.1016/j.nimb.2007.01.297>
- Noh, M.J. & Howat, I.M. (2015) Automated stereo-photogrammetric DEM generation at high latitudes: Surface Extraction with TIN-based Search-space Minimization (SETSM) validation and demonstration over glaciated regions. *GIScience and Remote Sensing*, 52, 198–217. <https://doi.org/10.1080/15481603.2015.1008621>
- Polcari, M., Albano, M., Atzori, S., Bignami, C. & Stramondo, S. (2018) The Causative fault of the 2016 Mwp 6.1 Petermann Ranges intraplate earthquake (central Australia) retrieved by C- and L-band InSAR data. *Remote Sensing*, 10, 1311. <https://doi.org/10.3390/rs10081311> [online] Available from: <http://www.mdpi.com/2072-4292/10/8/1311>
- Portenga, E.W. & Bierman, P.R. (2011) Data tables for understanding Earth's eroding surface with ^{10}Be . *GSA Today*, 21(8), 4–10. <https://doi.org/10.1130/G111A.1>
- Preiss, W.V. (2019) The tectonic history of Adelaide's scarp-forming faults. *Australian Journal of Earth Sciences*, 66, 305–365. <https://doi.org/10.1080/08120099.2018.1546228>
- Quigley, M.C., Clark, D. & Sandiford, M. (2010) Tectonic geomorphology of Australia. *Geological Society, London, Special Publications*, 346(1), 243–265. <https://doi.org/10.1144/SP346.13>
- Quigley, M.C., Cupper, M. & Sandiford, M. (2006) Quaternary faults of south-central Australia: Palaeoseismicity, slip rates and origin. *Australian Journal of Earth Sciences*, 53(2), 285–301. <https://doi.org/10.1080/08120090500499271>
- Quigley, M.C., Horton, T., Hellstrom, J.C., Cupper, M.L. & Sandiford, M. (2010) Holocene climate change in arid Australia from speleothem and alluvial records. *Holocene*, 20(7), 1093–1104. <https://doi.org/10.1177/0959683610369508>
- Quigley, M.C., Hughes, M.W., Bradley, B.A., van Ballegooij, S., Reid, C., Morgenroth, J. et al. (2016) The 2010–2011 Canterbury Earthquake Sequence: Environmental effects, seismic triggering thresholds and geologic legacy. *Tectonophysics*, 672–673, 228–274. <https://doi.org/10.1016/j.tecto.2016.01.044>
- Quigley, M.C., Sandiford, M., Fifield, L.K. & Alimanovic, A. (2007) Landscape responses to intraplate tectonism: Quantitative constraints from ^{10}Be nuclide abundances. *Earth and Planetary Science Letters*, 261, 120–133. <https://doi.org/10.1016/j.epsl.2007.06.020> [online] Available from: <http://linkinghub.elsevier.com/retrieve/pii/S0012821X07003962>
- Ramsey, B.C. (2008) Radiocarbon dating: Revolutions in understanding. *Archaeometry*, 50(2), 249–275. <https://doi.org/10.1111/j.1475-4754.2008.00394.x>
- Sandiford, M. (2003) Neotectonics of southeastern Australia: linking the Quaternary faulting record with seismicity and in situ stress. *Special Paper 372. Evolution and Dynamics of the Australian Plate*, 372, 107–119. <https://doi.org/10.1130/0-8137-2372-8.107> [online] Available from: <http://specialpapers.gsapubs.org/cgi/doi/10.1130/0-8137-2372-8.107>
- Sandiford, M. & Quigley, M.C. (2009) TOPO-OZ: Insights into the various modes of intraplate deformation in the Australian continent. *Tectonophysics*, 474, 405–416. <https://doi.org/10.1016/j.tecto.2009.01.028>
- Sandiford, M., Wallace, M. & Coblenz, D. (2004) Origin of the in situ stress field in south-eastern Australia. *Basin Research*, 16(3), 325–338. <https://doi.org/10.1111/j.1365-2117.2004.00235.x>
- Scrimgeour, I.R., Close, D.F. & Edgoose, C.J. (1999) *Petermann Ranges 1: 250 000 geological map*, Second edition. Darwin, NT: Northern Territory Geological Survey.
- Sieh, K.E. (1978) Prehistoric large earthquakes produced by slip on the San Andreas Fault at Pallett Creek, California. *Journal of Geophysical Research*, 83(B8), 3907. <https://doi.org/10.1029/jb083ib08p03907>
- Singh, G. & Luly, J. (1991) Changes in vegetation and seasonal climate since the last full glacial at Lake Frome, South Australia. *Palaeogeography, Palaeoclimatology, Palaeoecology*, 84(1–4), 75–86. [https://doi.org/10.1016/0031-0182\(91\)90036-Q](https://doi.org/10.1016/0031-0182(91)90036-Q)
- Small, E.E., Anderson, R.S., Repka, J.L. & Finkel, R.C. (1997) Erosion rates of alpine bedrock summit surfaces deduced from in situ ^{10}Be and ^{26}Al . *Earth and Planetary Science Letters*, 150(3–4), 413–425. [https://doi.org/10.1016/S0012-821X\(97\)00092-7](https://doi.org/10.1016/S0012-821X(97)00092-7)
- Stahl, T., Quigley, M.C., McGill, A. & Bebbington, M.S. (2016) Modeling earthquake moment magnitudes on imbricate reverse faults from paleoseismic data: Fox peak and forest creek faults, South Island, New Zealand. *Bulletin of the Seismological Society of America*, 106(5), 2345–2363. <https://doi.org/10.1785/0120150215>
- Stirling, M., Gerstenberger, M., Litchfield, N., McVerry, G., Smith, W., Pettinga, J. & Barnes, P. (2008) Seismic hazard of the Canterbury region, New Zealand: New earthquake source model and methodology. *Bulletin of the New Zealand Society for Earthquake Engineering*, 41(2), 51–67. <https://doi.org/10.5459/bnzsee.41.2.51-67>
- Stirling, M., Litchfield, N., Gerstenberger, M., Clark, D., Bradley, B., Beavan, J. et al. (2011) Preliminary probabilistic seismic hazard analysis of the co2crc Otway project site, Victoria, Australia. *Bulletin of the Seismological Society of America*, 101(6), 2726–2736. <https://doi.org/10.1785/0120110049>
- Stirling, M., McVerry, G., Gerstenberger, M., Litchfield, N., van Dissen, R., Berryman, K. et al. (2012) National seismic hazard model for New Zealand: 2010 update. *Bulletin of the Seismological Society of America*, 102(4), 1514–1542. <https://doi.org/10.1785/0120110170>

- Stone, J.O. (2000) Air pressure and cosmogenic isotope production. *Journal of Geophysical Research*, 105(B10), 23,753–23,759. <https://doi.org/10.1029/2000JB900181>
- Thom, R. (1971) A recent fault scarp in the Lort River area, Ravensthorpe 1: 250 000 sheet. In: *Geological Survey of Western Australia Annual Report 1971*. Perth, WA: Geological Survey of Western Australia, pp. 58–59 [online] Available from: <http://webapps.dpxe/search.jsp?cabinetId=1101&Combined=NAA71/12>.
- Tindall, S.E. & Davis, G.H. (1999) Monocline development by oblique-slip fault-propagation folding: The East Kaibab monocline, Colorado Plateau, Utah. *Journal of Structural Geology*, 21(10), 1303–1320. [https://doi.org/10.1016/S0191-8141\(99\)00089-9](https://doi.org/10.1016/S0191-8141(99)00089-9)
- Wang, S., Xu, W., Xu, C., Yin, Z., Bürgmann, R., Liu, L. & Jiang, G. (2019) Changes in groundwater level possibly encourage shallow earthquakes in central Australia: The 2016 Petermann Ranges earthquake. *Geophysical Research Letters*, 46, 3189–3198. <https://doi.org/10.1029/2018GL080510>
- Whitney, B.B., Clark, D., Hengesh, J.V. & Bierman, P. (2016) Paleoseismology of the Mount Narryer fault zone, Western Australia: A multistrand intraplate fault system. *Bulletin of the Geological Society of America*, 128(3–4), 684–704. <https://doi.org/10.1130/B31313.1>
- Williams, I.R. (1978) Recent fault scarps in the Mount Narryer area, byro 1: 250 000 sheet. In: *In Geological Survey of Western Australia Annual Report 1978*. Perth, WA: Geological Survey of Western Australia.
- Wintle, A.G. (1997) Luminescence dating: Laboratory procedures and protocols. *Radiation Measurements*, 27(5–6), 769–817. [https://doi.org/10.1016/S1350-4487\(97\)00220-5](https://doi.org/10.1016/S1350-4487(97)00220-5)
- Wobus, C., Helmsath, A., Whipple, K. & Hodges, K. (2005) Active out-of-sequence thrust faulting in the central Nepalese Himalaya. *Nature*, 434(7036), 1008–1011. <https://doi.org/10.1038/nature03499>
- Zielke, O. (2018) Earthquake recurrence and the resolution potential of tectono-geomorphic records. *Bulletin of the Seismological Society of America*, 108(3A), 1399–1413. <https://doi.org/10.1785/0120170241>
- Zondervan, A., Hauser, T.M., Kaiser, J., Kitchen, R.L., Turnbull, J.C. & West, J.G. (2015) XCAMS: The compact ^{14}C accelerator mass spectrometer extended for ^{10}Be and ^{26}Al at GNS Science, New Zealand. *Nuclear Instruments and Methods in Physics Research, Section B: Beam Interactions with Materials and Atoms*, 361, 25–33. <https://doi.org/10.1016/j.nimb.2015.03.013>

SUPPORTING INFORMATION

Additional supporting information may be found online in the Supporting Information section at the end of this article.

How to cite this article: King TR, Quigley M, Clark D, Zondervan A, May J-H, Alimanovic A. Paleoseismology of the 2016 M_{W} 6.1 Petermann earthquake source: Implications for intraplate earthquake behaviour and the geomorphic longevity of bedrock fault scarps in a low strain-rate cratonic region. *Earth Surf. Process. Landforms*. 2021;46:1238–1256. <https://doi.org/10.1002/esp.5090>